ISTANBUL TECHNICAL UNIVERSİTY ★ GRADUATE SCHOOL OF SCIENCE ENGINEERING AND TECHNOLOGY

FORMATION OF DENDRITIC SILICON-OXIDE STRUCTURES DURING CHEMICAL VAPOR DEPOSITION GROWTH OF GRAPHENE ON COPPER

M.Sc. THESIS

Umut KAMBER

Department of Physics Engineering

Physics Engineering Programme

FEBRUARY 2017

ISTANBUL TECHNICAL UNIVERSİTY ★ GRADUATE SCHOOL OF SCIENCE ENGINEERING AND TECHNOLOGY

FORMATION OF DENDRITIC SILICON-OXIDE STRUCTURES DURING CHEMICAL VAPOR DEPOSITION GROWTH OF GRAPHENE ON COPPER

M.Sc. THESIS

Umut KAMBER

509141126

Department of Physics Engineering

Physics Engineering Programme

Thesis Advisor: Assoc. Prof. Dr. Oğuzhan GÜRLÜ

FEBRUARY 2017

İSTANBUL TEKNİK ÜNİVERSİTESİ ★ FEN BİLİMLERİ ENSTİTÜSÜ

BAKIR ÜZERİNDE KİMYASAL BUHAR BİRİKTİRME İLE GRAFEN BÜYÜTME ESNASINDA AĞAÇSI SİLİKON-OKSİT YAPILARIN OLUŞUMU

YÜKSEK LİSANS TEZİ

Umut KAMBER

509141126

Fizik Mühendisliği Anabilim Dalı

Fizik Mühendisliği Programı

Tez Danışmanı: Doç. Dr. Oğuzhan GÜRLÜ

ŞUBAT 2017

Umut Kamber, a M.Sc. student of ITU Graduate School of Science Engineering and Technology student ID 509141126, successfully defended the thesis entitled "FORMATION OF DENDRITIC SILICON-OXIDE STRUCTURES DURING CHEMICAL VAPOR DEPOSITION GROWTH OF GRAPHENE ON COPPER", which he prepared after fulfilling the requirements specified in the associated legislations, before the jury whose signatures are below.

Thesis Advisor :	**Assoc. Prof. Dr. Oğuzhan Gürlü** Istanbul Technical University	.....
Jury Members :	**Assoc. Prof. Dr. Hakan Özgür Özer** Istanbul Technical University	.....
	Dr. Doğuş Özkan National Defense University	.....

Date of Submission : 10 February 2017
Date of Defense : 13 February 2017

To my family

FOREWORD

"Measure what can be measured, and make measurable what cannot be measured."
by Galileo Galilei

There are lots of people that I would like to thank. However, I owe a very special thank to my advisor Assoc. Prof. Dr. Oğuzhan Gürlü for his guidance, great support and friendship. I have learned many valuable things from him and I am sure that he will not give up to educate me.

It was my first step to science to be involved in nanoBEEs research group. I especially thank each one of my labmates for their help and patient support. It was really fun to work with you all.

Particularly, I thank to Cem Kıncal, my spiritual brother, and Altuğ Yıldırım for their precious friendship. Also, a very special thank goes to Dilek Yıldız, who is a former member of nanoBEEs and big sister for me. I thank to Kıvanç Esat for inspirational talks and discussions, which encouraged me all the time.

I owe a warm thank to Mehmet Çakıcı, a great engineer, and Yiğitcan Kahraman, future pilot and ex-physicist, for their friendship. I also thank to Anıl Anık even if he will not understand those lines. I know it was hard to share a home with me.

I would like to thank to Assoc. Prof. Dr. Özgür Birer and Dr. Barış Yağcı for their help and giving me an opportunity to use the laboratories in KOÇ University.

I thank to Assoc. Prof. Dr. Hakan Özgür Özer and Dr. Doğuş Özkan for evaluating my study.

I acknowledge TUBITAK because this work was supported by 1003 project with grant number 114F036.

Finally, I am grateful to my beloved family for their support in every period of my life.

"The deadline is yesterday."
by Oğuzhan Gürlü

February 2017

Umut Kamber
Engineer

TABLE OF CONTENTS

Page

ABBREVIATIONS

CVD	**:**	Chemical Vapor Deposition
Cu	**:**	Copper
STM	**:**	Scanning Tunneling Microscopy
Ni	**:**	Nickel
Pt	**:**	Platinum
C	**:**	Carbon
EDX	**:**	Energy Dispersive X-ray Spectroscopy
PE	**:**	Primary electrons
BSE	**:**	Backscattered electrons
SE	**:**	Secondary electrons
AFM	**:**	Atomic Force Microscopy
F_{TS}	**:**	Tip-surface forces
A	**:**	Amplitude
ϕ	**:**	Phase
f	**:**	Frequency
Q	**:**	Quality factor
LFM	**:**	Lateral Force Microscopy
MFC	**:**	Mass flow controller
Ru	**:**	Ruthenium
Ir	**:**	Iridium
Co	**:**	Cobalt
Pd	**:**	Palladium
IPA	**:**	Isopropyl alcohol
CH_4	**:**	Methane
H_2	**:**	Hydrogen
Ar	**:**	Argon
$FeCl_3$	**:**	Iron (III) chloride
SiO_2	**:**	Silicon dioxide
HOPG	**:**	Highly oriented pyrolytic graphite
G	**:**	Graphene
sccm	**:**	Standard cubic centimeters per minute

nm **:** nanometer

nN **:** nanonewton

LIST OF TABLES

Page

LIST OF FIGURES

Page

FORMATION OF DENDRITIC SILICON-OXIDE STRUCTURES DURING CHEMICAL VAPOR DEPOSITION GROWTH OF GRAPHENE ON COPPER

SUMMARY

Graphene is a two dimensional material with outstanding properties making it a promising material for future technological applications. It consists of carbon atoms in honeycomb lattice with sp^2 hybridization. Graphene has attracted intense attention of researchers due to extraordinary electronic, mechanical and optical properties as a consequence of its peculiar band structure. The desire of using graphene in daily-life technology led scientists to research on wafer scale production and further development of Chemical Vapor Deposition method for graphene. Growing graphene on metal substrates by decomposition of carbon containing molecules in gas phase is significant due to suitability for mass production. Thus, researchers have focused on optimizing CVD process to produce large area defect-free single layer graphene.

In this thesis, we focused on growing graphene by CVD method on relatively inexpensive polycrystalline copper foils. For the production of graphene by CVD, a new setup was built, which is suitable for both atmospheric and low-pressure conditions. Both full and partial coverage of single/multi-layer graphene were achieved on copper surfaces. Raman spectroscopy measurements were performed on samples to determine number of graphene layers. For the investigation on morphological and electronic properties of graphene, Scanning Tunneling Microscopy and Atomic Force Microscopy were performed under ambient conditions. Atomic scale characterization of graphene/Cu by STM resulted in the observation of honeycomb lattice of graphene as well as surface orientation of underlying copper substrate. Continuity and behavior of graphene layers over the step-edges of copper were investigated. Moiré patterns were observed on surfaces providing information about the interaction between graphene and copper.

On the other hand, during our study of optimizing CVD process, we encountered some droplet like impurities on surfaces. Such contaminations on CVD-grown graphene surfaces were commonly encountered silicon-oxide particles, generally believed to originate from quartz tube of the reactor or impurities in the bulk copper foils. While we tried to eliminate such contaminations by varying CVD process parameters, we discovered that it is possible to obtain even larger silicon-oxide particles on samples. As a result of experiments, we developed a methodology to produce different shapes and sizes of particles on surfaces. Moreover, we observed fractal formation of such contaminations on surfaces. The important parameters were determined to be hydrogen concentration in annealing atmosphere, annealing time and amount of methane dosing. Furthermore, we produced homogeneously distributed nano-scale silicon-oxide particles on bare Cu foils.

As a part of the study on the formation mechanism of fractal structures, we aimed at determining whether those particles were located at the graphene-Cu interface or on the graphene layer, since the shapes are determined by graphene formation. For that purpose, we used Lateral Force Microscopy, which is a method for measuring friction force between tip and surface by using cantilever bending.

BAKIR ÜZERİNDE KİMYASAL BUHAR BİRİKTİRME İLE GRAFEN BÜYÜTME ESNASINDA AĞAÇSI SİLİKON-OKSİT YAPILARIN OLUŞUMU

ÖZET

Grafen, üstün özellikleri sebebiyle ileri teknoloji uygulamalar için gelecek vaadeden iki boyutlu bir malzemedir. Karbon atomlarının bal peteği örgüsüyle dizilmeleri sonucu oluşur ve sp^2 hibridizasyona sahiptir. Alışılmamış bant yapısından kaynaklanan olağandışı mekanik, elektrik ve optik özellikleri yüzünden araştırmacıların ilgisini oldukça yoğun bir şekilde çekmiştir. Grafeni günlük hayatımızdaki teknolojik ürünlerde kullanma isteği araştırmacıları plaka boyutlarında grafen üretimine yöneltmiş ve Kimyasal Buhar Biriktirme (KBB) yönteminin grafen üretimi için modifiye edilmesine sebep olmuştur. Karbon içeren gaz fazındaki moleküllerin ayrıştırılması ile metal yüzeylerde grafen büyütmek, seri üretime yatkınlığı sebebiyle önemli hale gelmiştir. Bu sebeple, araştırmacılar kusursuz geniş alan grafen büyütmek için KBB yönteminin optimize edilmesi üzerine yoğunlaşmışlardır.

Bu tez çalışmasında düşük maliyetli bakır folyo üzerinde KBB yöntemiyle grafen büyütülmesine odaklanılmıştır. Bu amaç çerçevesinde, hem atmosferik hem de düşük basınçlarda çalışmaya uygun yeni bir KBB sistemi kurulmuştur. Kurulan yeni sistemin kalibrasyon çalışmalarından sonra, grafen üretilmesi için uygun parametlerin optimizasyonu çalışmıştır. Bu çalışmaların sonucunda bakır yüzeylerde tek ve çok katmanlı grafenin tamamen ve kısmen kaplanması başarılmıştır. Örnekler üzerindeki grafenin katman sayısını belirlemek için Raman spektroskopisi kullanılmıştır. Bunun haricinde, grafenin morfolojik ve elektronik özelliklerinin araştırılması amacıyla, laboratuar atmosferinde Taramalı Tünelleme Mikroskobu (TTM) ve Atomik Kuvvet Mikroskobu (AKM) çalışmaları gerçekleştirilmiştir. TTM ile yürütülen bakır üzerindeki grafenin atomik boyutlardaki araştırması ve karakterizasyonu sonucunda; bal peteği örgüsünün gözlenmesinin yanısıra grafenin altındaki bakırın yüzey yönelimleri de gözlenmiştir. Grafenin, bakır yüzeyinin basamak kenarları üzerindeki davranışı incelenmiş ve bu basamaklar üzerinde bütünlüğünü koruduğu görülmüştür. Ayrıca yüzey üzerinde moiré desenleri de gözlemlenmiştir. Bu desenlerin oluşması ve gözlenebilmesi grafen ve bakırın arasındaki etkileşim hakkında önemli bilgiler sağlamaktadır. Bunun haricinde TTM çalışmalarının laboratuar atmosferinde gerçekleştirilebilmesi ve bakır yüzeyinin basamak yüksekliklerinin atomik mertebede gözlenebilmesi, grafen katmanının bakır yüzeyini oksitlemekten koruduğunu göstermektedir.

Bu çalışmaların yanısıra, KBB yöntemiyle grafen büyütülmesinin optimizasyonu sırasında örnekler üzerinde küçük damlacıklar halinde safsızlıklar tespit edilmiştir. KBB ile büyütülen grafen üzerinde bu tarz silikon-oksit kirliliklerin sıklıkla karşılaşıldığı literatürde belirtilmektedir. Bununla beraber, literatürdeki hemen hemen her KBB metoduyla büyütülen grafen örnekler üzerinde bu safsızlıklar görülmektedir. Bu konudaki genel yargı, bu kirliliklerin ya bakır folyonun içerisindeki safsızlıktan ya da kuvartztan kaynaklandığıdır. Bu çalışmada, bu şekilde olan kirlilikleri oluşturmadan grafen büyütme çalışmaları KBB parametrelerinin değiştirilmesi ile gerçekleştirildi. Ayrıca, bu süreçte daha da büyük silikon-oksit parçacıkların oluşturulabildiği farkedildi. Yapılan kontrollü deneyler sonucunda, yüzey üzerinde farklı boyut ve şekillerde silikon-oksit parçacıklar

üretmek için yöntem geliştirdik. Üstelik bu kirliliklerin fraktal şeklinde de oluşabildiği gözlemlendi. Bu parçacıklar üzerinde etkili olan önemli parametreler; tavlama atmosferindeki hidrojen miktarı, tavlama süresi ve büyütme atmosferindeki metan miktarı olarak belirlendi. Bunlara ek olarak, bakır folyo üzerinde homojen olarak tüm yüzeye dağılmış silikon-oksit nanoparçacıklar üretildi.

KBB ile grafen büyütülmesi işlemi sırasında bakır folyoların tavlanması önemli bir aşamadır. Yapılan deneyler sonucunda tavlama atmosferindeki hidrojen miktarı ve tavlama süresi, örnek yüzeyinde biriken silikon miktarını ciddi bir şekilde etkilemektedir. Tavlama atmosferindeki hidrojen miktarının artışı ile birlikte tavlama süresinin uzaması da örnek yüzeyindeki silikon-oksit miktranın ciddi bir şekilde artmasına sebep olmaktadır. Bunun yanısıra, yüzeyde toplanan silikonların boyut ve şekillerini etkileyen faktör büyütme atmosferindeki metan gazının miktarı ve büyütme süresi olarak belirlenmiştir. Büyütme atmosferindeki metan miktarı ve büyütme süresi yüzeyde grafen oluşma mekanizmasını önemli bir şekilde etkilediği ve işlem sonucunda oluşan grafenin katman sayısı ve tek pul boyutu gibi özelliklerini değiştirdiği bilinmektedir. Bu sebeple, aslında grafenin oluşumu parçacıkların son şeklinin belirlenmesini sağlamaktadır.

Yapılan çalışmalar sonucunda literatürde karşılaşılanlardan daha büyük ve daha çok silikon-oksit parçacık üretilmesi, silikonların kaynağının sadece bakır folyo içindeki safsızlıklar olamayacağını göstermiştir. Bu konuda yapılan hesaplar, folyo içindeki safsızlıklar haricinde başka bir kaynağın olması gerektiğini göstermiştir. Kuvartz malzemesi KBB reaktöründeki tek silikon içeren malzeme olduğundan, silikonların kuvartzdan kaynaklandığı düşünülmektedir. Kuvartz malzemeden silikon salınımının nasıl ve neden olması gerektiği hakkında bazı fikirler ortaya atılmıştır.

Parçacıkların miktarına etkiyen faktörlerin bulunmasını haricinde, fractal yapıdaki parçacıkların oluşum mekanizması da incelenmiştir. Bu parçacıkların oluşma mekanizmasının anlaşılması için yapılan çalışmalar kapsamında, parçacıkların grafen katmanının üzerinde mi yoksa grafen ile bakır arayüzünde mi olduğu incelendi. Yani, grafenin varlığının ve oluşum mekanizmasını bu parçacıkların şekillerini belirlediği tespit edildiği için, grafenin hangi şekilde etki yaptığı tespit edilmeye çalışılmıştır. Grafen katmanının parçacıkların üzerini kaplayıp kaplamadığı bilgisinin bu parçacıkların oluşum mekanizmasının açıklanmasına katkısının olacağı şüphesizdir.

Bu incelemenin yapılmasında tip ve yüzey arasındaki sürtünme kuvvetini ölçen Sürtünme Kuvvet Mikroskobu (SKM) kullanılmıştır. Bu araştırma sırasında SKM kalibrasyonu yapılmış, ve ölçülen SKM manivelası bükülmelerinden tip-yüzey arasındaki sürtünme kuvvetinin nasıl hesaplanacağı çalışılmıştır. Bu hesaplamaların ardından örnekler üzerinde sürtünme kuvveti ölçümleri yapılmış ve ilk olarak grafensiz silikon-oksit parçacıkların oluştuğu örnek üzerinde referans ölçümleri yapılmıştır. Bu referans ölçümleri bize tip ve silikon-oksit parçacıkların arasındaki sürtünme kuvvetini vermiştir. Böylece, hem grafen hem de silikon-oksit parçacık içeren örnekler üzerinde yapacağımız SKM çalışmasının sonuçları bu referans ölçümleriyle karşılaştırılmış ve fraktal parçacıkların grafen ile kaplı olup olmadığı incelenmiştir. Yapılan tüm deneylerde SKM parametreleri sabit tutulmuş ve sürtünme değerleri kendi örneklerimiz arasında karşılaştırılmıştır.

Silikon-oksit parçacıklar üzerinde yapılan SKM çalışması sonucunda, nokta şeklindeki parçacıkların grafen katmanı altında, yani grafen-bakır arayüzünde, olduğu belirlenmiştir. Fraktal parçacıkların ise grafen-bakır arayüzünde mi yoksa grafenin üstünde mi olduğu bulunduğu bölgenin katman sayısıyla ilgili olabileceği gözlenmiştir. Bu sonuçlar ışığında silikonların yüzeye geldikten sonra bir araya toplanması ve farklı şekillerde parçacıklar oluşturması grafen-bakır arayüzünde meydana geldiği tahmin edilmiştir.

1. INTRODUCTION

1.1 Graphene

Carbon is a unique element because of the possibility to form a lot of allotropes. The most common allotropes of carbon are graphite and diamond, which are known since ancient times. By the end of past century, a spherical molecule, which consists of 60 carbon atoms "the buckyball", and cylindrical nanostructures "the carbon nanotubes" were introduced [1-3]. Two-dimensional case of graphite, which contains carbon atoms in a honeycomb lattice were studied theoretically in 1947 by Wallace [4]. The 2D form of graphite was named as *graphene* by Boehm in 1994 [5]. Graphene attracted great attention from many scientists due to its peculiar band structure that allows it to have extraordinary electronic, mechanical and optical properties. Due to linear dispersion relation near K-point, charge carriers behave as Dirac fermions (zero effective mass) in graphene [6,7]. Half-integer quantum Hall Effect was observed in single layer graphene [8,9]. Moreover, it is well known that graphene has an absorption of 2.3% of visible light, although being composed of a single layer of carbon atoms. [10].

Many techniques were developed for experimental realization of graphene. In 2005, Geim and Novoselov achieved to obtain single layer mechanically exfoliated graphene and measured several expected properties [11,12]. This invention brought them a Nobel Prize *"for groundbreaking experiments regarding the two-dimensional material graphene"* in 2010 [13]. After this, many researchers focused on production of graphene and possible daily-life applications. Large amount of studies were published in recent years. This led to the birth of the 2D materials era.

1.2 Purpose of Thesis

Since using graphene in technological applications requires a mass production at the wafer scale, Chemical Vapor Deposition (CVD) method was modified for graphene production and presented as a convenient technique for this purpose. In this work, we focused on CVD growth of graphene on copper surface and characterization of it from atomic scale to micro scale with several experimental methods. We first aimed to achieve growth of

graphene on polycrystalline copper foils by both atmospheric and low-pressure CVD. After the growth was achieved in both systems with full and partial graphene coverage, we studied behaviour of graphene on copper at the atomic scale and interaction between them. However, rather than the atomic scale characterization, there are other apparent factors affecting the quality of graphene growth. It has been known since the first CVD growth of graphene on Cu foils in a quartz tube that there were some droplet like silicon-oxide contaminants appearing on the graphene layers [14-18]. We focused on the reason and formation mechanism of such contaminations on surfaces.

1.3 Literature Review

Large amount of studies were published in recent years about CVD grown graphene. In this section, the focus will be on probe microscopy investigation of CVD-grown graphene and observation of silicon-oxide impurities. One of the most important STM studies about the behavior of CVD-grown graphene on copper was performed by Rasool [15, 19]. They acquired clear STM images of honeycomb lattice of graphene on copper surfaces under ambient conditions. Also copper step-edges under graphene were observed and measured. Almost in every CVD-grown graphene study, silicon-oxide impurities were observed but not mentioned clearly [14-18]. It is possible to see them even in the first study that reported graphene growth by CVD on copper [14]. Later, these were attributed to silicon or silicon oxide contaminations [20-22]. Most of the researchers believe that bulk copper cause them. A recent study about direct observation of graphene growth by CVD showed that such particles occur on the copper surface before releasing methane, when the temperature reached to about 850 °C in the CVD reactor and they were shown to be mobile at that temperature [21]. Another recent study showed that they can be in bunches of dendritic form [22].

2. EXPERIMENTAL METHODS

2.1 Chemical Vapor Deposition

Chemical Vapor Deposition (CVD) is a widely used process for producing high quality thin films. Thin graphite layer formation on transition metals has been known for around 50 years using this method [23-26]. Observation of graphite layers on both Ni, by exposing to hydrocarbons [24,27], and Pt [28,29] were reported before. Also, graphite formation on copper was unintentionally achieved in 1991, however somehow missed by recent literature [30,31]. The interest in graphene led to the modification of these methods for graphene production.

In the CVD process, metal substrates to be coated are heated up and precursor gases are released into the chamber. Chemical reactions occur on the hot surface and result in deposition of a thin film. It is possible to produce graphene by chemical vapor deposition. Although mechanical exfoliation of graphene results high quality single layer graphene crystal with nearly ideal electrical properties, producing wafer scale graphene with this technique is not possible. Because of the possibility to produce large area graphene, CVD is presented as the most convenient production method for graphene.

Mechanism of chemical vapor deposition growth includes several steps. First of all, precursor gas diffuse through the boundary layer between surface and gas mix and reach the surface. Generally, methane (CH_4) or ethylene (C_2H_4) is used for production of graphene. When they reach the surface, they decompose to form active carbon species such as CH or C. They diffuse on the metal surface to form graphene lattice. Meanwhile, inactive species, hydrogen, get desorbed from the surface [32,33].

2.2 Spectroscopy Techniques

2.2.1 Raman spectroscopy

Raman spectroscopy is a technique based on inelastic scattering of monochromatic light. One interpretation of Raman scattering is, photons are absorbed and then reemitted after interaction with molecular vibrations, phonons or other excitations in sample. Due to the

energy and momentum transfer between incident photon and sample, emitted photon can be more or less energetic than the incident photon. Thus, the frequency of reemitted photon is shifted. Since the shift in frequency provides information about vibrational modes, it is a commonly employed method in material characterization [34-36].

Raman shifts are generally expressed in wavenumbers. It is directly related to wavelength;

$$\Delta\omega = (\frac{1}{\lambda_0} - \frac{1}{\lambda_1}) \quad (2.1)$$

where $\Delta\omega$ is the Raman shift expressed in wavenumber (cm^{-1}), λ_0 and λ_1 are wavelengths of incident and reemitted photon [34].

2.2.2 Energy Dispersive X-Ray Spectroscopy

Energy Dispersive X-ray Spectroscopy (EDX) is an elemental analysis technique used for chemical characterization. In this technique, inner shell of an atom is ionized by exciting an electron due to inelastic collision between incident electron and inner shell electron. After that, another electron from higher energy state fills the vacancy in inner shell. The high-energy electron must release some of its energy to fill the vacancy. Due to energy difference between these two states, X-ray is emitted [37-40].

Electrons in an atom occupy in orbitals with specific energies defined by principle quantum numbers (n). The closest shell to the nucleus (n=1) is known as K shell and n=2 shell is called the L shell. By basic quantum mechanics, each shell has certain number of states. Ejecting a K-shell electron creates a vacancy. This causes an L shell electron to lower its state to K shell. Since the energies of two states are different, radiation occurs related with energy difference. Radiation caused by removing an electron from L shell to K shell is in the X-ray range of the spectrum. Since this energy difference between these shells are characteristic for each element, X-ray radiation provides chemical information [37-40].

EDX systems are mostly attached to Electron Microscopy systems. By adding an X-ray spectrometer, an Electron Microscopy system can also be used for elemental analysis. We used Zeiss Ultra Plus microscope and Bruker Quantax EDX system with a Bruker Xflash 5010 X-ray detector.

2.3 Microscopy Techniques

2.3.1 Scanning Electron Microscopy

In Scanning Electron Microscopy the surface is scanned with a focused electron beam. It is a widely used technique to investigate microstructures on surfaces [41]. Since wavelength of a particle is defined by de Broglie relation, the wavelength of electrons in the beam can be expressed by [42];

$$\lambda_e = \frac{h}{\sqrt{2m_e eV_{acc}}} \tag{2.2}$$

where, h is Planck constant in unit of J.s and V_{acc} is accelerating voltage of electrons. Since the wavelength of electrons in the beam is a function of accelerating voltage, it is possible to decrease wavelength by increasing the voltage to obtain better resolution.

When the incident beam of electrons, called primary electrons (PE), penetrate into surface, various types of signals can be produced due to both elastic and inelastic collisions [37]. All possible signals that can be produced after penetration of PE is shown in Figure 2.1.

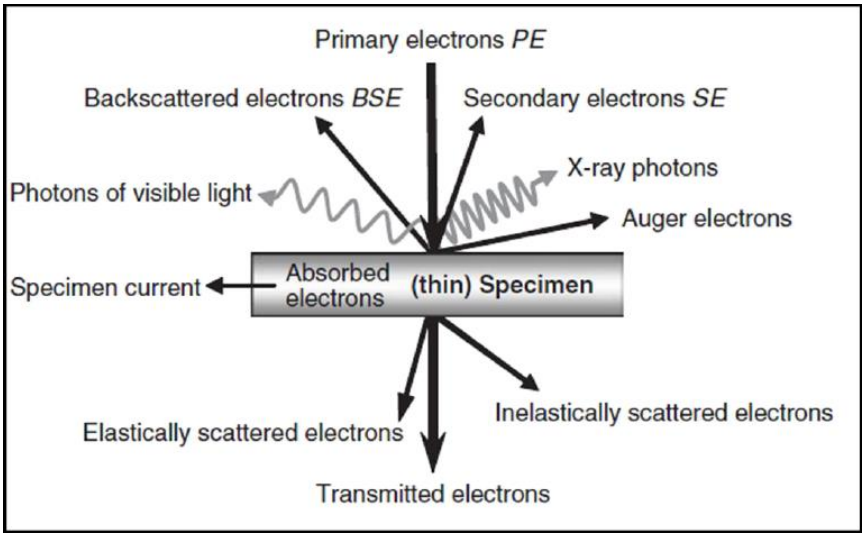

Figure 2.1 : All possible signals produced after penetration of PE [43].

Elastic collisions of PE with the sample atoms result in backscatter electrons (BSE) from the sample surface. Since the kinetic energy is conserved in elastic collisions, backscatter electron signal has the higher energy. BSE provide a contrast between chemical

compositions due to the fact that scattering angle is a function of atomic number of scattered atom. Brightness of BSE image provide information about atomic number of the specimen [37].

Furthermore, PE can also excite the electronic transitions of the sample atoms by making inelastic collisions with them. Secondary electrons (SE), Auger electrons and X-ray emission can be produced due to inelastic collision. Secondary electrons provides information about surface topography [37,39,43].

2.3.2 Scanning Tunneling Microscopy

Scanning Tunneling Microscopy (STM), almost the first member of scanning probe microscopy family (first being the filled emission scanning microscopy or commonly known as the Young's scanner [44]), is an instrument to investigate surfaces of both conducting and semiconducting materials at atomic scale. It was invented in 1981 by Gerd Binnig and Heinrich Rohrer at IBM Zürich [45]. After five years from the invention, design of STM brought them Nobel Prize. [46]. Invention of STM opened a new era in surface science by giving birth to probe microscopy. Several types of probe microscopy were developed in following years to measure different properties of surfaces by using the key feature of their invention, which is a feedback loop regulating the distance between probe and the surface.

STM is based on the quantum tunneling principle, which explains the possibility of an electron passing through an energy barrier, which has higher energy than electron has. In quantum theory, motion of an electron is described by Schrödinger equation [47]. According to solution of Schrödinger equation with appropriate boundary conditions, electron is not allowed to be in the barrier, however there exist solutions in both sides of the barrier. The fact that electron passing to the other side of the barrier without being in it is called quantum tunneling. A representative image of quantum tunneling in STM is shown in Figure 2.2. The idea of using this phenomenon as a microscopy technique involves creating tunneling current between a very sharp tip and biased sample surfaces by letting electrons tunnel and using the tunneling current as a feedback parameter to map electron density of states of the scanned surface. [48,49].

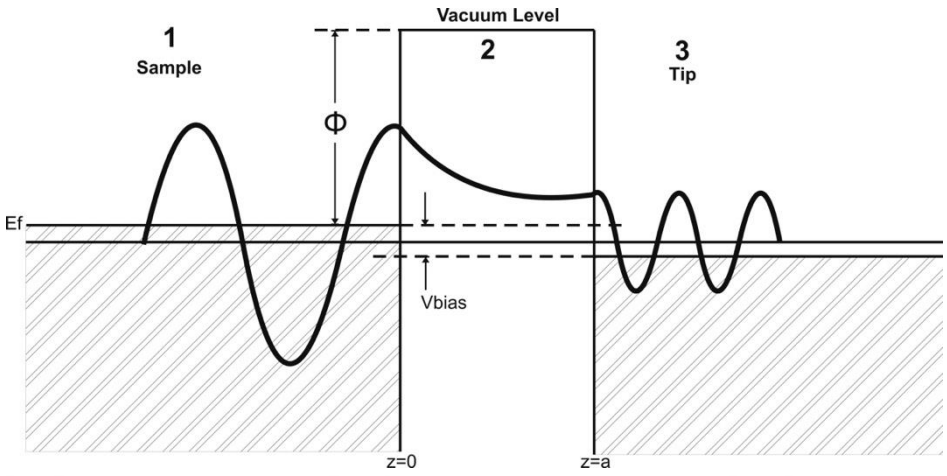

Figure 2.2 : Representative image of quantum tunneling from the sample to the tip in Scanning Tunneling Microscopy. The gap between sample and tip behaves as potential barrier in region 2.

$$I_{tunneling} \approx \sum_{E_f - V_{bias}}^{E_f} |\psi(0)|^2 e^{-1.025\sqrt{\phi}z} \approx V\rho_s(0, E_f)e^{-1.025\sqrt{\phi}z} \qquad (2.3)$$

In order to obtain tunneling current, an atomically sharp conducting tip is brought close to the sample surface (less than 1 nm distance). An applied bias voltage between the tip and the sample allows electrons to tunnel through a gap between them. As a result of this, tunneling current occurs as a function of gap distance, applied bias voltage and local density of states of the surface as expressed in equation 2.3 [48]. Once the tunneling current obtained, bias voltage and gap distance can be varied depending on experiment and resulting change in the tunneling current can be measured. To vary the gap distance and also scan the surface in xy-plane, piezoelectric material is used. Lateral resolution of STM tip is in sub-angstrom range due to the sensitivity of piezoelectric material. Since the tunneling current is exponentially related with to the gap distance, small variations in distance z greatly affect the tunneling current as expressed in equation 2.3. Therefore, z resolution of STM is in the sub-picometer range.

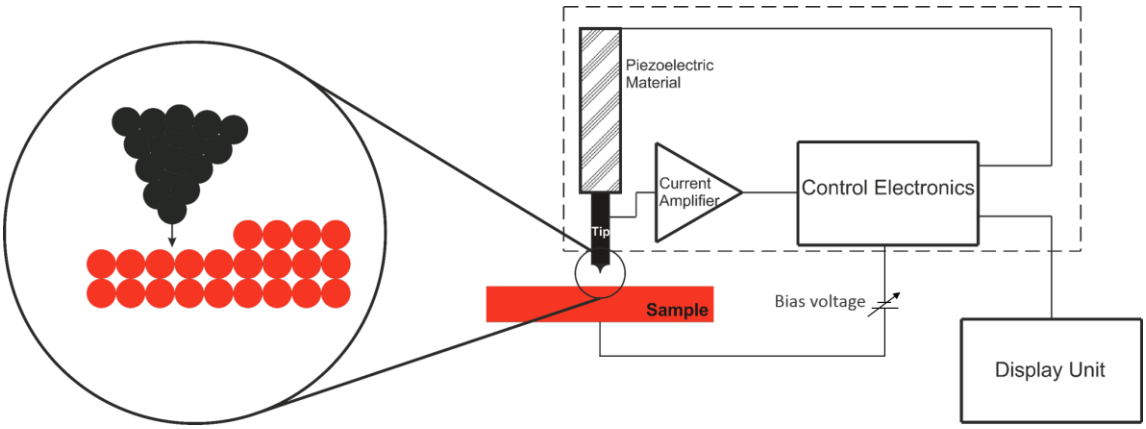

Figure 2.3 : A scheme of Scanning Tunneling Microscopy.

There are two main scanning modes in STM depending on the parameter that is kept constant. One of them is achieved by keeping the height of the tip constant and called constant height mode. During the scanning over surface, gap distance and observed electron density of states of the sample can change because of the morphological and electronic structure of the surface. Thus, the changes affect the tunneling current. Recording and mapping the tunneling current gives topographic information on the surface.

Another mode is achieved by keeping tunneling current constant during scanning the surface. Constant current mode STM application requires a feedback loop. In this mode, gap distance between tip and the surface is varied by using the tunneling current as the feedback parameter. During the scan, at each point, relative height is changed due to electronic and morphological structure of the sample surface. This causes a change in tunneling current. To keep the tunneling current constant, relative height between tip and surface is changed by applying voltage to the piezoelectric material which sample mounted on. As a result, topography of the surface is generated by mapping the voltage applied to the piezoelectric material in z direction.

2.3.3 Atomic Force Microscopy

As STM relies on measuring a tunneling current between the tip and the sample, it limits the variety of measurable materials to conductors and semiconductors. Because of that, development of probe microscopy turned towards to imaging surface of insulator materials with a resolution as high as STM. In 1986, the effort led to the invention of

Atomic Force Microscopy, which can be applied on a large variety of surfaces by measuring the interatomic forces between the tip mounted on a cantilever and surface [50].

If two neutral atoms or molecules are brought close to each other, an interaction force occurs between them. This force may be attractive or repulsive depending on the separation distance and charging characteristic of the atoms and molecules. If the separation distance between them is about few nanometers, attractive forces become dominant. If they are brought closer, their electron clouds start to overlap. Because of the Pauli principle, repulsive force increases and becomes dominant. The summation of these attractive and repulsive interactions are called Lennard-Jones Potential, which gives all interactions between two neutral atoms as a function of separation distance [51-53].

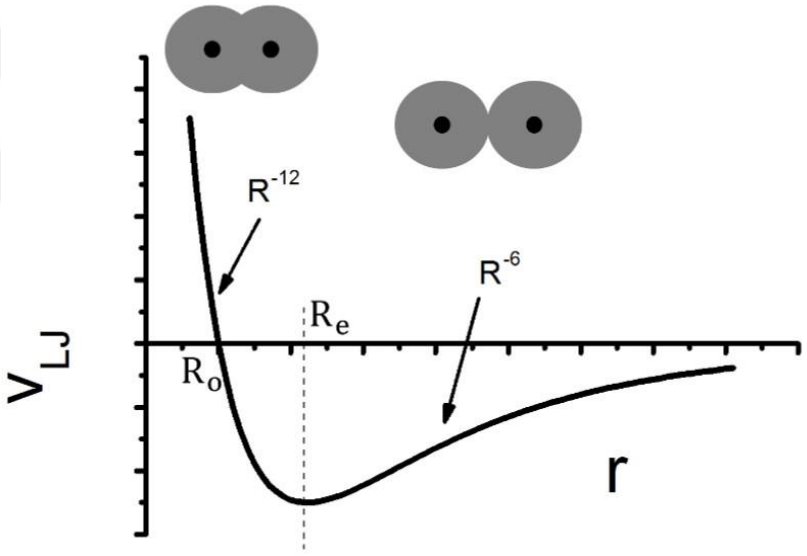

Figure 2.4 : Lennard-Jones potential showing summation of all possible interactions between two neutral atoms. [53]

$$V_{LJ} = \frac{a}{r^{12}} - \frac{c}{r^{6}} \tag{2.4}$$

AFM measures forces by using a cantilever with a tip attached to the free end of it. When the tip approaches to the surface, due to the atomic interaction explained above, cantilever bends. In the most basic form, AFM measures the forces using the bending of cantilever. Therefore, feedback parameter of AFM is the bending of a cantilever. In Figure 2.5, a simple scheme of AFM is shown.

In order to measure the bending of the cantilever, a deflection sensor system is used. This system includes a laser beam focused on the end of cantilever and a photodiode at the trajectory of reflected beam from cantilever. The photodiode has been split to four segments having precise alignments. Voltage differences between all segments give the deflection data of cantilever. The voltage difference between left and right segments of photodiode gives lateral bending, similarly between up and down segments gives normal bending.

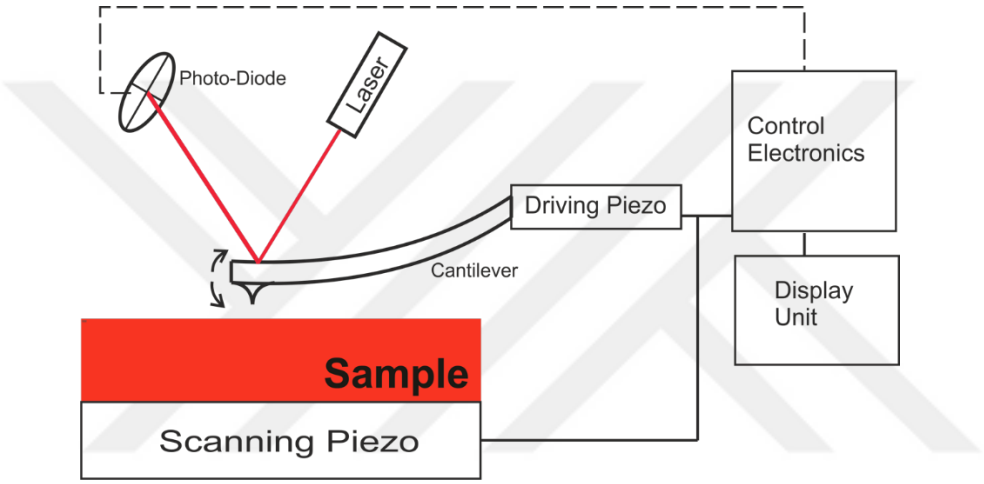

Figure 2.5 : A simple scheme of Atomic Force Microscopy.

Mainly there are two types of AFM operation: Static and dynamic modes. In the static mode operation, the tip is kept in contact with the surface while scanning. Surface morphology is obtained by mapping the cantilever bending in normal direction. It is important to mention that there is not a feedback loop in this operation mode. Static mode AFM works in the repulsive region of the Lennard-Jones potential. However, elasticity of cantilever is very important in this type operation. Since the tip is always in contact with surface, it is possible to damage the tip or surface while scanning due to surface roughness. Static mode AFM is quite unsafe method to obtain morphology of the surface. However, keeping the tip in contact with surface is required for some special cases such as friction measurements.

In order to overcome damaging risk of both tip and sample surface, dynamic mode operation was developed. In this case, cantilever is forced to oscillate at/near its resonance frequency by an additional piezoelectric material attached to the cantilever. During the

oscillation, cantilever can be considered as a spring, thus the motion can be modeled as damped harmonic oscillator. In this case, measureable variables with the help of deflection sensing system are amplitude (A), frequency (f) and phase (ϕ) of the oscillation.

While the cantilever oscillates freely and if interaction starts between tip and surface by getting cantilever closer to the surface, then additional force (F_{TS}) affects the oscillation of the tip. Due to additional driving force caused by tip-surface interaction, characteristics of free oscillation vary. Either amplitude or frequency of the oscillation can be used as feedback parameter. It is needed to precisely tune frequency with small amplitudes for frequency modulation applications to obtain atomic resolution without touching the surface. However, it is not possible under ambient condition. Tuning relatively large amplitudes and using it as feedback parameter is more suitable for under ambient applications. We used amplitude modulation dynamic mode AFM for our most experiments. When the amplitude of free oscillation is shifted because of the additional tip-surface interaction, this shift is detected by photodiode and scanning piezo moves the sample according to keep amplitude constant. Mapping the voltage applied on scanning piezo gives the morphology of the surface.

The dynamics of the cantilever behind this operation is important. The equation of motion of the cantilever at free space can be expressed as [54,55];

$$\frac{\partial^2 z}{\partial t^2} + \gamma \frac{\partial z}{\partial t} + \omega_0^2 z = \frac{F_0}{m}\cos(\omega t) \tag{2.5}$$

Amplitude and phase of oscillation can be written as;

$$A = \frac{F_0}{m\sqrt{\left(\omega_0^2 - \omega^2\right)^2 + \left(\frac{\omega\omega_0}{Q}\right)^2}} \tag{2.6}$$

$$\phi = \arctan\left(\frac{\frac{\omega\omega_0}{Q}}{\omega_0^2 - \omega^2}\right) \tag{2.7}$$

where $Q = \frac{\omega_0}{\gamma}$, defined as the quality factor. After the interaction starts between tip and surface, by introducing additional force, the equation motion becomes;

$$\frac{\partial^2 z}{\partial t^2} + \gamma \frac{\partial z}{\partial t} + \omega_0^2 z = \frac{F_0}{m}\cos(\omega t) + F_{TS} \tag{2.8}$$

Then, amplitude and phase terms can be expressed as [54,56];

$$A \approx A_0 \sqrt{1 - 4\left(\frac{F_{TS}}{F_0}\right)^2} \tag{2.9}$$

$$\phi = \arctan\left(\frac{k}{Q\sum \frac{\partial F_{TSi}}{\partial z}}\right) \tag{2.10}$$

As it can be seen above, characteristics of the oscillation are changed according to tip-surface interaction.

2.3.4 Lateral Force Microscopy

Since the tip and surface are in contact in static mode AFM operation, there occurs friction force between them while scanning the surface. Scanning along perpendicular to the cantilever axis causes torsional bending of the cantilever, which can be measured by voltage difference between left and right segments of photodiode [57-59]. If the dimensions and stiffness of cantilever are known, friction force that act on tip can be calculated.

$$F_l = k_l S_l \Delta V \tag{2.11}$$

The relation between voltage difference and friction force is shown in equation 2.11, where F_l is lateral force, k_l is lateral force constant of cantilever in unit of N/m, S_l is lateral deflection sensitivity in unit of m/V and ΔV is measured voltage difference from photodiode in unit of Volts.

The lateral deflection sensitivity of photodiode should be defined. It can be calculated by using normal deflection sensitivity, which is obtained by force-distance spectroscopy on hard and stiff surfaces. Force-distance spectroscopy is a method that measures the bending of cantilever in normal direction while tip is approaching to the surface. In Figure 2.6 (b), an example of F-D spectroscopy performed on Si(100) surface was shown. The tip is starting to approach to the surface from its rest position (z=0). At its rest position, tip is far away from the sample and any interaction does not occur between them. Until the

contact point, which is about at 500 nm according to spectroscopy data, deflection of cantilever is zero. After contact, voltage difference starts to increase indicating bending of cantilever.

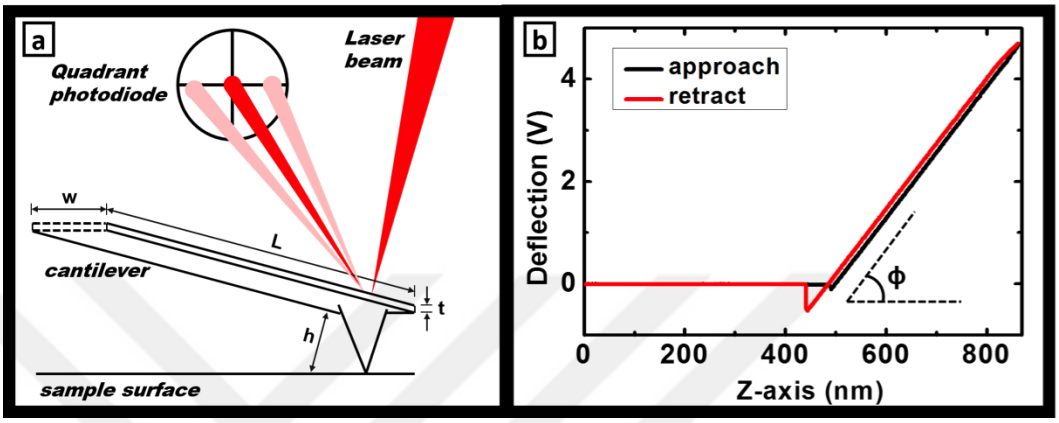

Figure 2.6 : (a) Scheme of AFM cantilever is shown with the dimensions. Incoming laser beam and reflection from it onto the quadrant photodiode is shown. (b) Performed Force-distance spectroscopy on Si(100) surface is given.

Normal deflection sensitivity of photodiode is obtained from $\cot(\phi)$ of force-distance spectroscopy and lateral deflection sensitivity can be calculated as;

$$S_l = \frac{E\left(h+\frac{t}{2}\right)}{2GL}\cot(\phi) \tag{2.12}$$

Where E is Young's modulus, G is shear modulus, h is height of the tip from cantilever, w is width, t is thickness and L is length of cantilever [60].

Here, the factor $\frac{E\left(h+\frac{t}{2}\right)}{2GL}$ result from the fact that same deflection in normal and lateral directions cause different angular motion of cantilever. Another constant that must be known in equation 2.13 is the lateral force constant of cantilever. Force constant for bending a one end fixed cantilever in lateral direction can be calculated as [60];

$$k_l = \frac{Gwt^3}{3L\left(h+\frac{t}{2}\right)^2} \tag{2.13}$$

Table 2.1 : The properties of PPP-CONTSCR cantilever designed for contact mode applications [61].

Property	Nominal value	Specified range
Thickness (um)	1	0.1-2.0
Mean width (um)	48	40-55
Length (um)	225	215-235
Resonance frequency (kHz)	23	1-57
Guaranteed tip radius of curvature (nm)	<10	-
Tip height (um)	10-15	-
Force constant (N/m)	0.2	-

After the calculations, one can find the lateral force acting on the tip by using voltage difference in the lateral electrodes of photodiode. However, lateral bending of cantilever can result from not due to local differences in the friction coefficient on surfaces, but also morphological effects (Figure 2.7). In order to obtain friction related bending of the cantilever, morphological effects must be eliminated. In Figure 2.7, two possible cases of lateral bending are shown. In the first case (Figure 2.7 a), there is a hill on the surface without any material difference (also no friction coefficient). While the tip scans on one side of the hill, surface force ($F_{surface}$), which bends the cantilever, has two components while one of them in lateral direction (F_y). In this case, scanning in forward and backward directions results green and blue lines, which is shown in Figure 2.7 (a). The offset between lines are resulted from the fact that the tip is already bent due to friction between surface and the tip. In the second case, there is a region that has higher friction coefficient (μ_2) than the rest of surface (μ_1) without any morphological difference. Forward and backward scan lines are reverse of each other in this case, since the direction of friction force is depended on direction of motion (Figure 2.7 b).

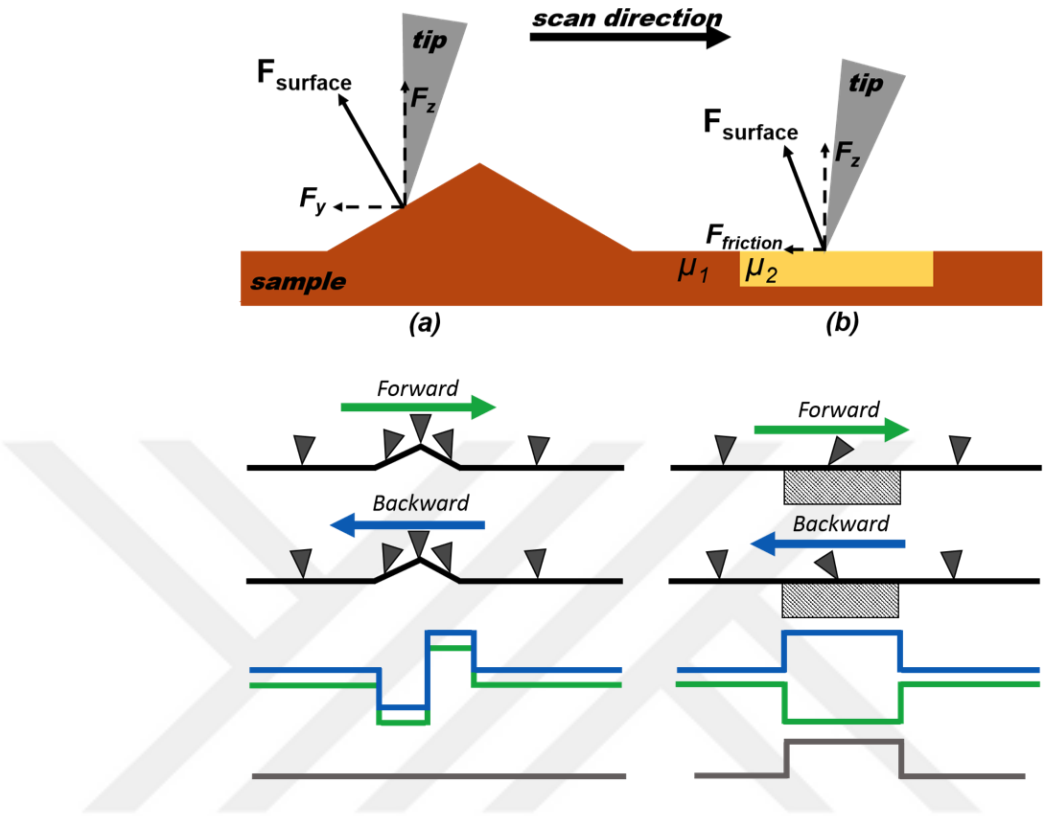

Figure 2.7 : Two possible cases for lateral bending of the cantilever with components of surface force is shown. Green and Blue lines in both case (a) and (b) represent Forward and Backward scanning lines. Grey lines are the results of mathematical expression given in Equation 2.14.

Elimination of morphological effects was achieved by subtracting forward and backward lines from each other, then dividing by two. Due to the fact that forward and backward scanning are the same in first case (Figure 2.7a), subtraction result a straight line (grey line in Figure 2.7a). Subtraction in second case (Figure 2.7b) gives the difference of friction coefficients on the surface.

$$\frac{|\,\mathrm{def}_{bwd} - \mathrm{def}_{fwd}\,|}{2} \tag{2.14}$$

By using this simple relation, it is possible to obtain friction coefficient difference on surfaces, which is generally caused by material composition differences.

3. SAMPLE PREPARATION

3.1 Chemical Vapor Deposition Growth of Graphene

3.1.1 Setup

We have an atmospheric pressure Chemical Vapor Deposition setup with a tube oven that we used before for graphene growth experiments. During this work, we built a new CVD setup for graphene growth, which is suitable for both atmospheric and low pressure studies. Heating was provided by a split oven, which can be heated up to 1100 °C with a cylindrical heating region length of 30 cm and diameter of 10 cm. We used a quartz tube as the reaction chamber and quartz plate to place samples in the center of the tube. Total volume of the reaction chamber is 7.5 liters. The reasons to use quartz are, its resistivity to thermal shock and stability at high temperatures.

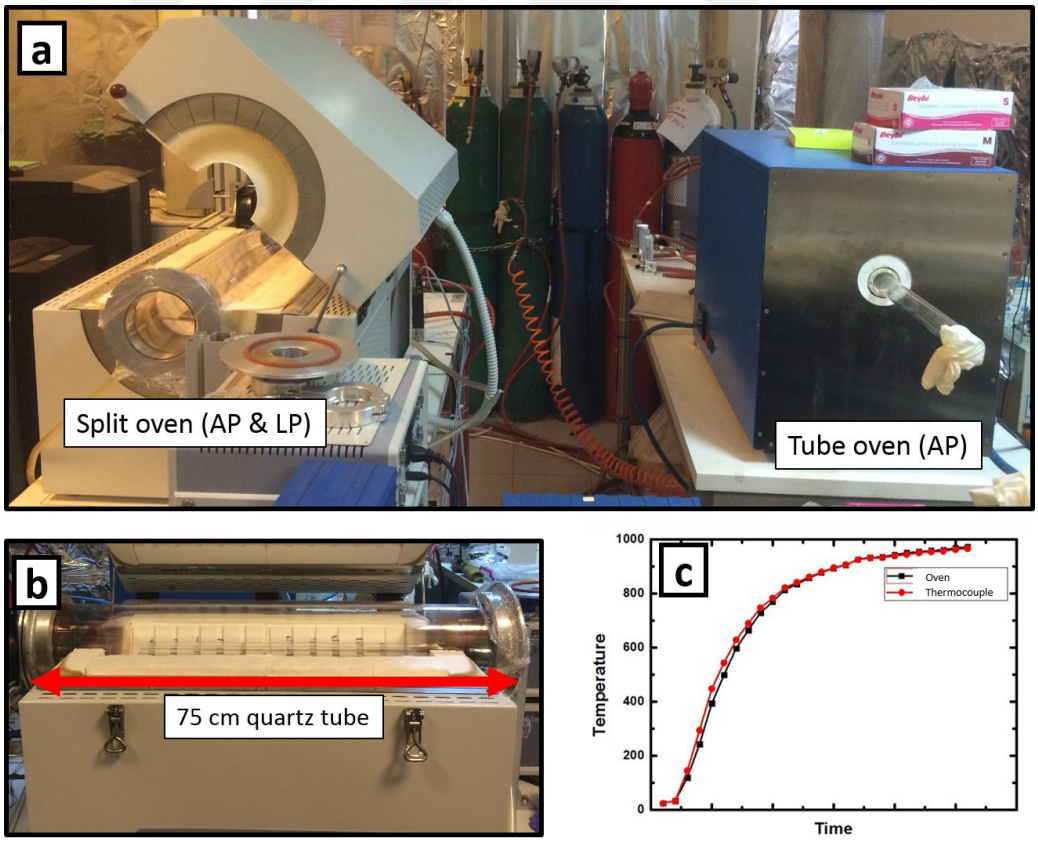

Figure 3.1 : (a) Image of two CVD setups in our laboratory. (b) Image of new setup which built for both AP & LP CVD applications. (c) Heating test of split oven is shown.

In order to control the atmosphere inside the chamber, Teledyne HFC computer controlled Mass Flow Controllers (MFC) were used. The MFCs were controlled by a Terralab software. As a gas carrier system, stainless still tube lines were installed from main gas tanks to CVD system. Also purge lines were installed in front of MFCs in order to purge remaining gasses from previous experiment.

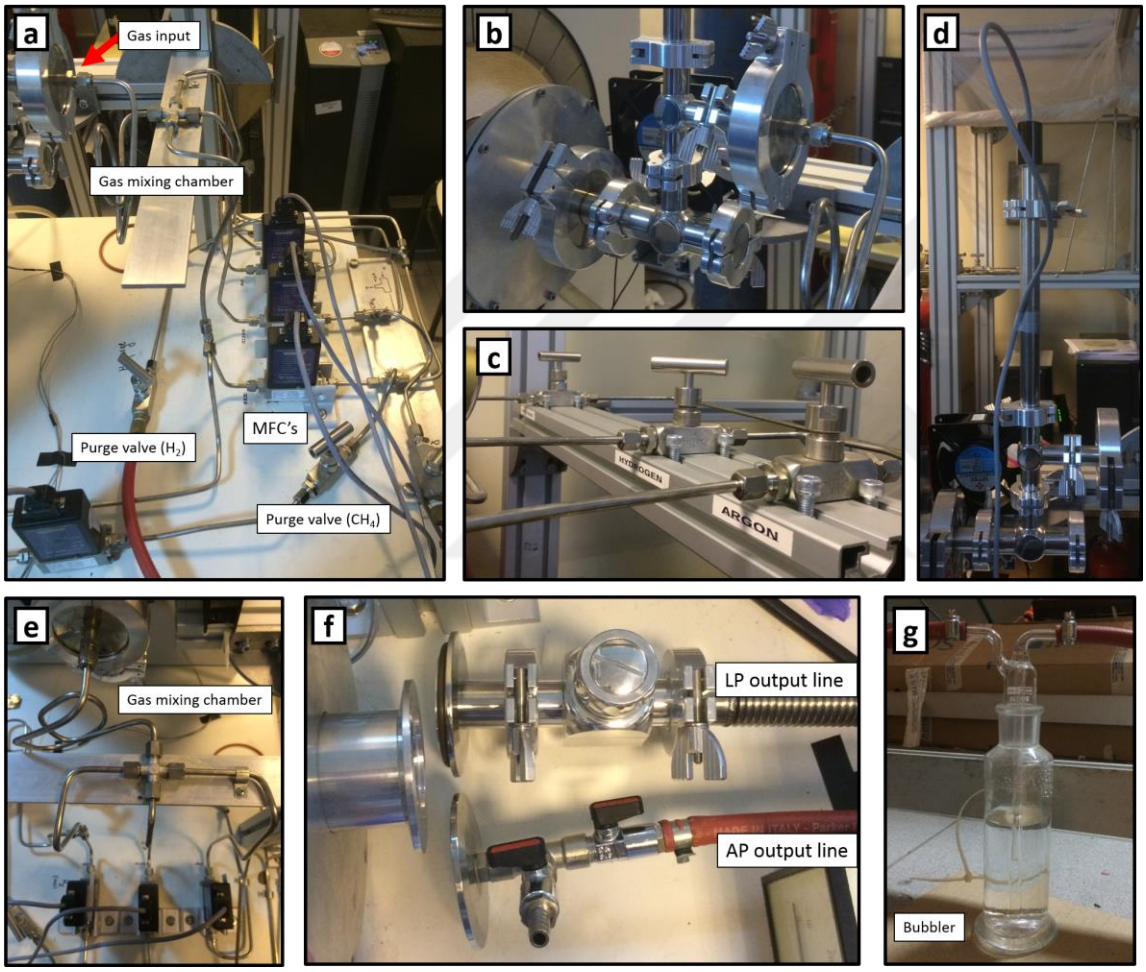

Figure 3.2 : (a) Image of gas input system of CVD setup. (b) Connection of stainless steel line and quartz tube. (c) Gas valves for each gas are shown. Images of (d) Piriani gauge for monitoring pressure inside the chamber and (e) gas mixing chamber. (f) Output lines for gas handling parts are shown.

To make the setup suitable for both atmospheric and low-pressure applications, we installed two different gas handling parts. For the atmospheric pressure applications, output line is connected to a gas washing bottle (Figure 3.2 g) and for low-pressure application, there is a rotary vane pump with 8 lt/min pumping rate instead of bubbler. A piriani gauge is used for monitoring pressure (Figure 3.2 d).

3.1.2 Substrates

Thermal decomposition of methane occurs at high temperatures (> 1200 °C) due to strong bonds between carbon and hydrogen. In order to reduce the temperature, catalytic property of transition metals is used in graphene production by decomposition of methane [62]. Partially filled d-orbitals of transition metals provides low energy pathways for active species on surface during the reaction [63,64]. Graphene growth on metal surfaces is a catalytic process and deposition mechanism is strongly related with carbon solubility and crystal structure of substrate [23]. By taking into the account these factors, several transition metals are used for graphene production via decomposition of hydrocarbons on the surface, such as Ru, Ir, Co, Ni, Pt, Pd [65-72]. In recent years, achievement of graphene growth on relatively inexpensive Cu and Ni foils attracted great attention for the purpose of optimizing CVD growth of graphene. Since copper is suitable for the growth of several carbon allotropes such as graphite, diamond, carbon nanotubes, it is also one of the best substrates for graphene growth by decomposition of hydrocarbons [14, 73-77].

Due to low solubility of carbon in copper, it does not form any carbide phases [19, 20]. Solubility of carbon in copper is very low (about 0.004 weight % at around 1084 °C) compared to nickel (about 0.6 weight % at 1326 °C) [78,79]. Thus, synthesis of graphene is limited to surface [23, 80]. Additionally, 3d-shell of copper is filled, which is most stable configuration due to symmetric electron distribution. As a result of this, only weak bonds occur between copper and carbon caused by charge transfer between π electrons in the sp^2-hybridized carbon and 4s state of copper [81,82].

Samples were cut into pieces in various sizes (Figure 3.3a) and dipped into IPA before placing in the CVD chamber. Polycrystalline copper foils have varying surface roughness including large protrusions due to manufacturing process, grain boundaries occurring at high temperatures because of polycrystalline nature and steps formed due to misorientation of high and low index facets. Manufacturing protrusions became smoother after annealing but it is not possible to completely eliminate them [17].

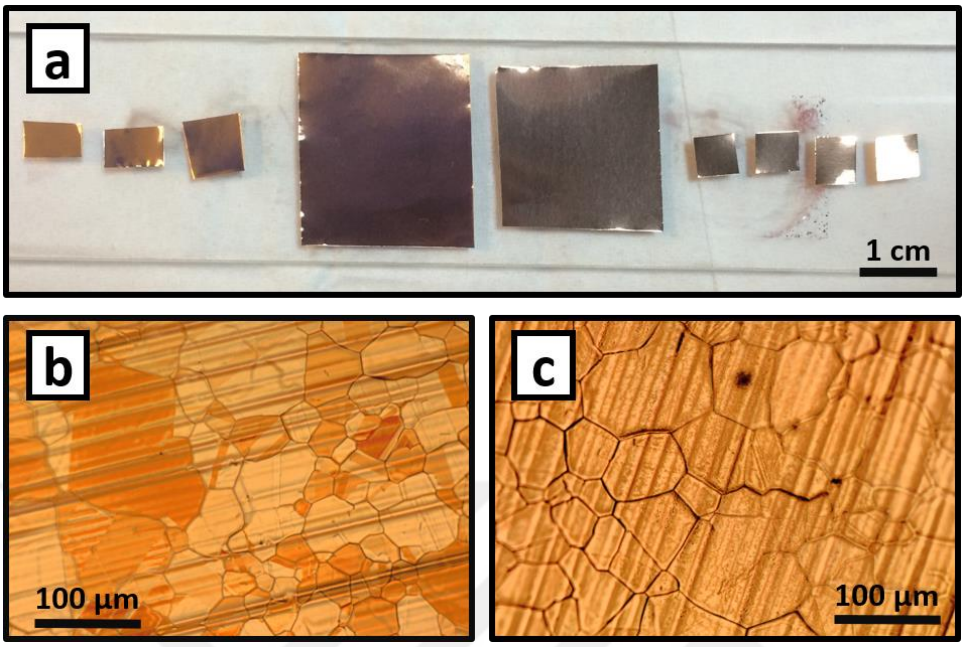

Figure 3.3: (a) Image of copper foil samples on quartz plate. Optical images of copper foils after CVD process (b) without and (c) with methane exposure.

3.1.3 Growth atmosphere and background pressure

Graphene growth on transition metals is a catalytic process which contains three main steps; adsorption of hydrocarbons on metal surface, decomposition of them to form active carbon species and aggregation of these species on surface to form final graphene structure [62]. In our case, hydrocarbon is methane molecule and transition metal used as substrate is copper. Before discussing the growth kinetics of graphene, it is better to mention that exact nature of active carbon species on the substrate has not been determined yet [23].

Since the copper has a role as catalytic surface for dehydrogenation of CH_4 molecules, the overall reaction for graphene formation on copper surface by decomposition of methane can be expressed as [83];

- $CH_4 + Cu \rightarrow Graphene + 2H_2$

This overall reaction includes three individual reversible steps causing final graphene structure. First step is dehydrogenation reactions from CH_4 to monoatomic carbon and four hydrogen. [83, 17, 84];

- $CH_4 + Cu \leftrightarrow CH_3 + H$
- $CH_3 + Cu \leftrightarrow CH_2 + H$
- $CH_2 + Cu \leftrightarrow CH + H$
- $CH + Cu \leftrightarrow C + H$

However, complete dehydrogenation of methane is very difficult on copper, since carbon dimers or partially dehydrogenated species ($CH_{x<4}$) are more stable than C adatoms. Therefore, it is expected that active species contain hydrogen at early stage of graphene growth [17,84-86]. Following the decomposition of methane, while diffusion of active species starts on surface, desorption of inactive species happens as the second step of overall reaction [83, 87];

- $4H \leftrightarrow 2H_2 + Cu$

One of the essential points of CVD process for graphene production is supplement of additional hydrogen gas in to the reactor. First of all, copper foils must be annealed in hydrogen-reducing atmosphere in order to eliminate native oxide layer, which reduces its catalytic activity. Annealing also helps to re-arrangement of the surface and by increasing copper grain sizes. On the other hand, it is stated that hydrogen acts as an activator of surface-bound carbon species and dehydrogenation of methane is not favorable on copper without the presence of hydrogen. Since the reaction for desorption of inactive H is reversible, role of hydrogen as activator can be illustrated by [87].;

- $CH_4 + H \leftrightarrow CH_3 + H_2$

Hydrogen also has a role as an etching reagent to control the size and number of graphene flakes, since hydrogen can etch carbonaceous materials [84,87,88]. In the absence of additional methane supplement in to the reaction chamber, the etching of graphene by hydrogen is expected due to the fact that dehydrogenation reaction is reversible [83].

Experimental observations state that growth rate increases with the decrease of hydrogen concentration, high CH_4/H_2 ratio. Lower CH_4/H_2 ratio leads to lower nucleation density and higher quality of graphene [89]. Since high hydrogen concentration in growth

atmosphere decrease the nucleation density, higher hydrogen concentrations may prevent graphene formation on surface.

The third and final step of overall reaction is aggregation of active carbon species on copper surface to form final graphene structure. This step can be illustrated by [83];

- $C \leftrightarrow graphene$

Stability of active carbon species on surface is strongly related with crystal structure of the substrate. Since copper substrates are polycrystalline foils, diffusion mechanism is varying on the surface according to grains. For example, atomic carbon is more stable on Cu(100) than on Cu(111). Thus, diffusion of active species is faster on Cu(111), leading increase in number of nucleation center [84].

Besides the growth atmosphere and properties of substrate, background pressure is also a critical parameter due to changing the kinetics of growth while thermodynamics remain same [32,90]. One disadvantage of low pressure is increasing the copper sublimation. High sublimation rate of copper causes instability of the surface, which affects the adsorption mechanism of carbon species negatively. On the other hand, in atmospheric pressure CVD, high amount of argon is used as a buffer gas in order to obtain inert atmosphere. In this case, desorption of inactive species from surface is decreased due to collision with buffer gas. Higher returning rate of desorbed species to the surface disturb the diffusion of carbon species on surface and cause defects [90,91].

First step of the graphene growth by CVD is obtaining the growth atmosphere, after the copper foils were prepared and placed into CVD chamber. For low-pressure applications, chamber is pumped and small amount of argon is used to regulate the pressure at desired value. For growth under atmospheric pressure, high amount of argon is used to remove atmospheric gases and obtain an inert atmosphere. Then, by releasing hydrogen into the chamber, annealing atmosphere is obtained. The system is heated up to annealing temperature and copper foils were annealed under hydrogen and argon atmosphere in both AP and LP CVD. After the annealing, graphene growth process is triggered by releasing methane in to the chamber [Appendix A].

3.2 Transfer of Graphene on to Arbitrary Substrates

Since graphene is required to be on a dielectric substrate for many electronic applications, CVD grown graphene on metal substrates must be transferred on to arbitrary surfaces. Although there are many studies on transfer of graphene, creation of defects on graphene during the process as well as polymer residue and contaminations resulting from chemicals are still unsolved problems. In our study, we used PMMA based wet transfer method which is one of the most common methods for transferring CVD grown graphene on to dielectric substrates [92]. Steps of transfer procedure include in general; coating the desired side of graphene/copper sample with PMMA (polymethyl-methacrylate) etching and removing the copper substrate in $FeCl_3$ solution, scooping out PMMA/graphene system with desired substrate and removing PMMA in acetone bath (Figure 3.4).

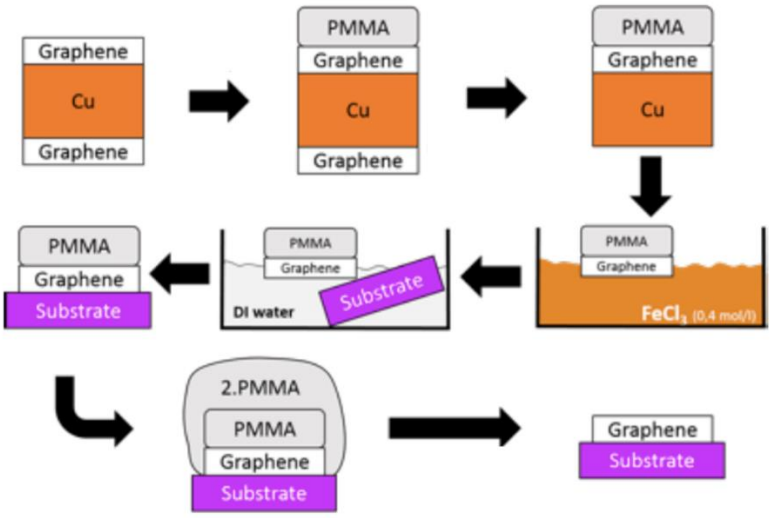

Figure 3.4 : Schematic steps of transfer process of graphene from copper to arbitrary substrate is shown.

We spin-coated (1000 rpm, for 30 seconds) our samples with (8 mg/ml) PMMA/Acetone solution and cured at room temperature for 12 hours. Since graphene grow on both sides of copper foil in the CVD process, graphene on the backside of the sample was removed by polishing. Following, copper was removed by etching in (0.4 mol/l) FeCl3 solution. After the copper was completely etched, $FeCl_3$ solution was diluted by adding de-ionized water in to the bath. Floating PMMA/graphene sample was scooped out with desired

substrate and kept at room temperature for 12 hours, in order to make sure that all of the intercalated water between wafer and graphene was vaporized. Finally, PMMA/graphene sample left in acetone bath to remove PMMA. After eliminating PMMA on the sample, transferring process of graphene on wafer completed. Optical images of as-grown graphene/copper and transferred graphene/SiO_2 are shown in Figure 4.1 (a, b).

4. CHARACTERIZATION OF GRAPHENE

4.1 Raman Spectrum of Graphene

Raman spectroscopy is a useful inspection tool to determine number of graphene layers on the surface. Raman spectra of graphene was studied theoretically and experimentally before and major features were determined. According to previous studies, fingerprint of graphene involves peaks appearing at 1582 cm^{-1}, called G-band, as an indicator of graphitic material and at about 2700 cm^{-1} called G'-band using laser excitation at 2.41 eV. In addition to that, another peak at 1350 cm^{-1} can appear corresponding to disordered sample, called D-band [36,93].

At room temperature, G' peak of CVD-grown graphene shows a single Lorentzian feature with full width half maximum of between 24-38 cm^{-1}. Intensity ratio of G and G' peak provide a correlation with number of graphene layers. In the spectra of single layer graphene, G' peak is roughly four times higher than G peak [93]. After third layer of graphene, G peak become more intense than G' peak. Moreover, in trilayer graphene case, full width half maximum of Lorentzian G' peak is about 80 cm^{-1} [36].

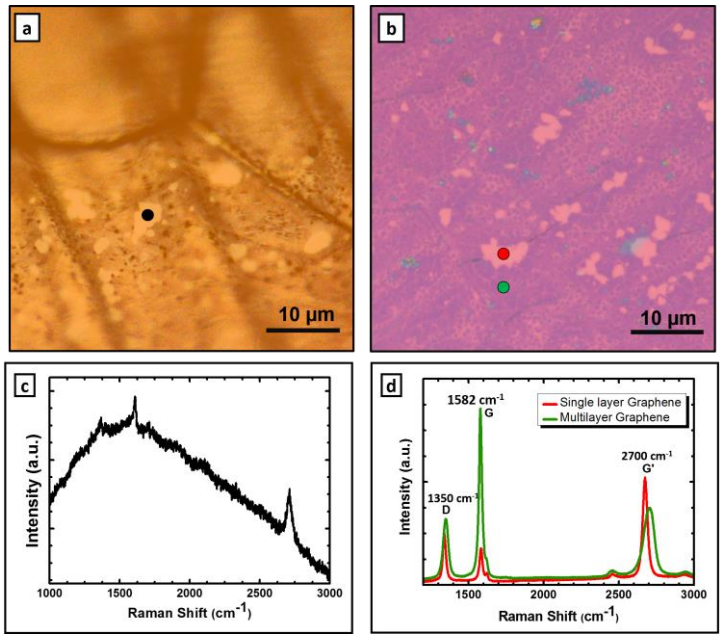

Figure 4.1 : Optical images of (a) graphene on copper and (b) transferred graphene on SiO_2 wafer. (c) Raman spectrum of single layer graphene on copper. (d) Raman spectra of single and multilayer graphene on SiO_2 wafer.

Due to the surface roughness and strong fluorescence background of metal substrates, analyzing Raman spectrum of graphene on copper system is difficult. In order to avoid this, we transferred the graphene onto SiO_2 wafer. In Figure 4.1, Raman spectrums of multi and single layer graphene are shown. In Raman spectrum of single layer graphene, marked with red dot in figure, intensity ratio of G and G' peaks (I'_G/I_G) is 3 with 30 cm^{-1} full width half maximum of G' peak. In the region marked with green dot, G peak is higher than G' peak indicating multilayer graphene.

4.2 Scanning Electron Microscopy study on graphene

After single/multi-layer regions on graphene/Cu sample were determined, Scanning Electron Microscopy investigation was performed. An example of SEM image at the focusing single-multi layer graphene boundary is shown in Figure 4.2. Bright area in Figure 4.2 (b) corresponds to single layer graphene according to comparison with optical microscopy and Raman spectroscopy results. It has to be noted that graphene reflectivity to electrons is a function of the number of layers. Although single layer graphene may look bright and bilayer graphene may appear darker in SEM images, trilayer graphene may be brighter than the monolayer graphene [94]. When we zoomed to the boundary (Figure 4.2 d), we observed wrinkles of graphene in the multilayer region and order of underlying copper substrate in single layer region. Also, in Figure 4.2 (c), green circle indicates silicon-oxide contaminations on surface.

We were also able to grow graphene partially by LP-CVD process. In Figure 4.3, optical and SEM images of partial grown graphene on copper is shown. In contrast to fully graphene coverage case, darker areas correspond to graphene and bright regions are copper surface. Since Raman analysis has not been performed on partially growth graphene samples yet, we do not have information about number of layers. However, order of underlying copper substrate under graphene can again be seen in Figure 4.3 (c), allowing us to assume it is single layer graphene by comparing with fully graphene covered samples. Observation of copper surface ordering under graphene covered regions shows that graphene formation protect copper surface from oxidation.

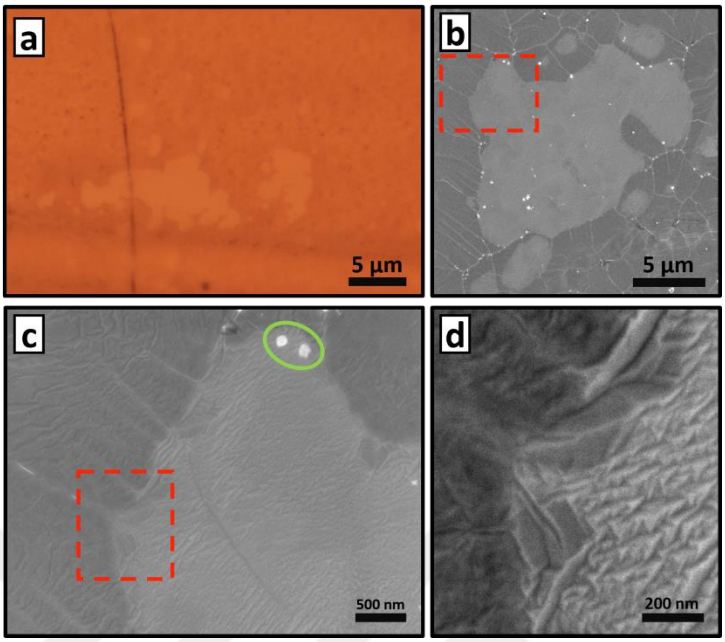

Figure 4.2 : (a) Optical image and (b, c, d) Scanning Electron Micrographs of graphene/Cu sample. Bright areas correspond to single layer graphene according to Raman analysis. Crystallization of copper substrate can be seen in bright area of (d) (V_{acc} = 2 kV for all SEM images).

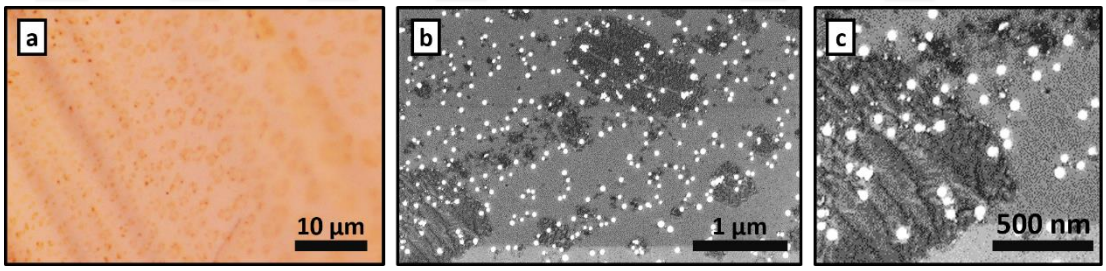

Figure 4.3 : (a) Optical image and (b, c) Scanning Electron Micrographs of partially grown graphene/Cu sample by LP-CVD (V_{acc} = 2 kV for all SEM images).

4.3 Probe microscopy investigation

Probe microscopy provides atomic scale surface information. Observation of the honeycomb lattice is possible by probing single layer graphene. Additionally, we aimed to observe several characteristics of graphene and interaction with underlying substrate, such as behaviour of graphene at the step-edges of copper substrate. Ambient-STM study was performed on samples for these purposes.

A Nanosurf Easyscan2^{TM} STM, which is very useful for investigating conductive surfaces with user-friendly software, was used. We used Platinum-Iridium (%80-%20) alloy wire

with a diameter of 0.25 mm for a tip. Tips were prepared by mechanical cutting. WSxM and Gwyddion softwares were used for analyzing data [95].

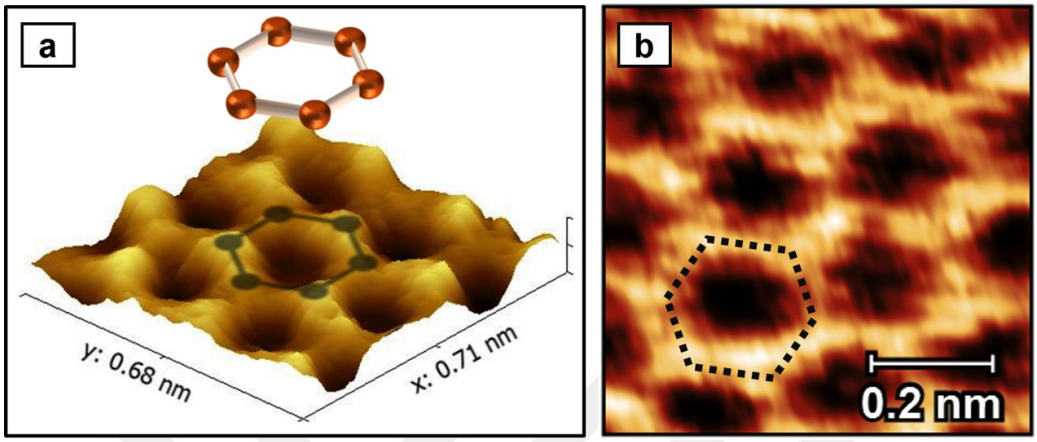

Figure 4.4 : Scanning Tunneling Microscopy measurements under ambient conditions on graphene/Cu sample is shown. (a) 3D visualization of graphene surface obtained by ambient STM data in (b) section.

In Figure 4.4, honeycomb lattice of graphene, hexagonal structure of carbon atoms, on copper can be seen. Since STM observes the high density of states (DOS) regions, not only atoms but also bonds between the carbon atoms can be observed. 3D visualization of graphene surface was obtained by STM data given in Figure 4.4 (b). A model of single hexagonal graphene and projection of the model is shown.

As the first result, we have shown that graphene layer protects underlying copper surface from oxidization. In Figure 4.5, STM data of graphene on two different copper surfaces are shown. Since copper foils have polycrystalline nature, after the annealing, several types of surface orientations can form. It is possible to predict underlying copper crystalline surface by measuring step heights. Measured step heights corresponding to single step of Cu(111) in Figure 4.5 (a) and Cu(110) in Figure 4.5 (b) are shown. For measuring step heights, roughness analysis is a very common method and it provides a good average. It shows us how many points were measured at which height. By fitting a Gaussian to histograms, centers of these peaks were measured and the difference between two centers gives the step height of between those two terraces.

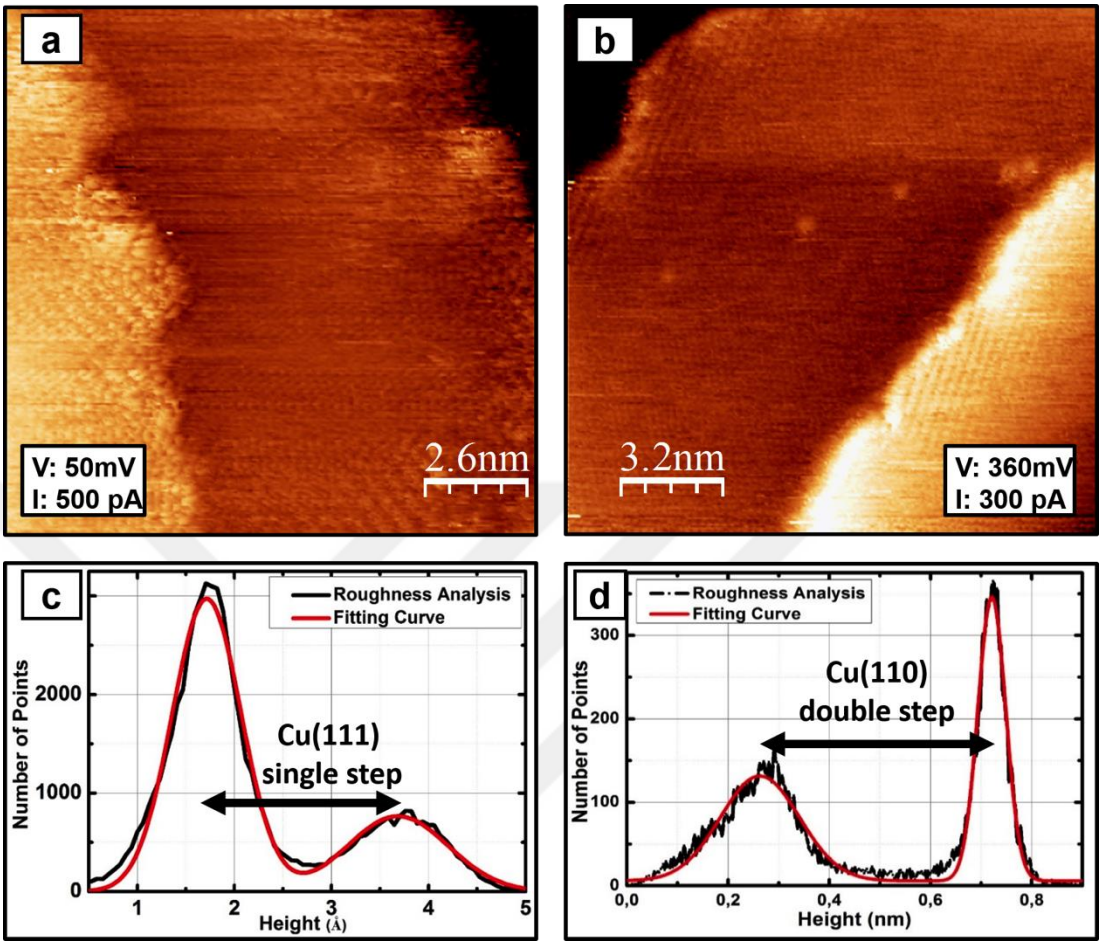

Figure 4.5 : (a, b) Large scale STM measurements on graphene/Cu sample showing single steps of underlying copper surface. (c, d) Height histogram analysis of STM data given in a and b is shown. Corresponding copper orientation according to height histogram analysis is given on the graphs.

Observing single copper steps with STM under ambient conditions is important. Since copper surface instantly oxidizes under atmospheric ambient, it is not possible to measure single step height on bare copper, or even to tunnel on to it with an STM. However, graphene acts as a protective layer and we were able to measure single steps of copper surface. In addition to that it shows us the continuity of graphene layer over the surface and over the step edges. This topic was studied before and continuity of graphene over step-edges was reported [19].

On the other hand, at room temperature, it is known that copper steps are mobile because of the high mobility of edge atoms. However, we did not observe any diffusion in our studies. It means that graphene also pins the copper steps and prevent step diffusion.

Ambient STM study of graphene on copper gives important information about the interaction between graphene and copper, which is still unclear. Graphene stands on the copper and the interaction between them is strong enough to pin the copper step diffusion [15, 19].

Another observation, which gives information about the interaction between graphene and copper is the moiré patterns occurring on surfaces. Moiré patterns can be seen in our daily life as an optical illusion and they are caused by rotation/shift of one periodic pattern on another (Figure 4.6 a,b). However, observing moiré patterns in STM images is an extra-ordinary event. It is not possible to see any optical illusion in STM images, since we measure mostly electron density. Such patterns were studied before on HOPG surface, which is a stack of graphene layers. The explanation of the observation of moiré patterns on graphite (or graphene) is the rotation of the topmost layer with respect to the rest of the crystal. The formation of moiré patterns and physics behind them is currently being studied [96].

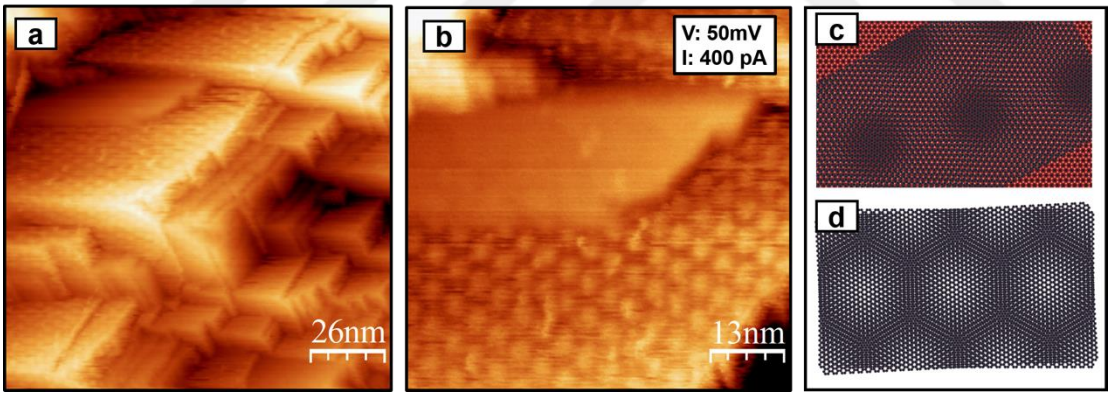

Figure 4.6 : (a) STM measurement on graphene/Cu sample. (b) Zoomed STM data in section (a) showing moiré patterns. (c, d) Two possible models for obtaining moiré patterns observed in section (b).

We observed moiré patterns on graphene on copper (G/Cu) system. It may be possible to predict underlying copper surface crystal orientation by measuring the pattern periodicity. However, if the pattern caused by two hexagonal layers like Cu (111) and graphene, it is not possible to distinguish that the pattern cause by G/Cu or bilayer G/G case. As example to that, in Figure 4.6, STM data of observed moiré pattern and some models are shown. According to measured periodicity of moiré patterns, which is 5 nm, we created two

different models; one of them is the rotation of single layer G on Cu(111) surface by 27,5° rotation angle (Figure 4.6 c), the other one is rotation of single G layer on another G layer by 3° rotation angle (Figure 4.6 d). It is possible to obtain same moiré pattern in two cases.

$$D = \frac{pa}{\sqrt{1+p^2-2pcos(\theta)}} \tag{4.1}$$

Where D is moiré periodicity, p is the ratio between lattice constants, a is lattice constant of substrate and θ is rotation angle [97, 98].

On the other hand, in Figure 4.6 (a), it can be seen that on some terraces there is not any moiré pattern. If we assume that the pattern is caused by G/Cu (111), we can say that interaction of G-Cu is dependent on terrace. Or if we assume G/G moiré pattern, we can say that some terraces are tend to grow multilayer graphene.

For further morphological characterization of the surfaces, we performed dynamic mode AFM measurements on samples. In Figure 4.7, SEM image of single-multi layer graphene boundary and AFM measurements on single layer graphene regions are shown. As mentioned before, in SEM study section, order of underlying copper substrate can be observable under single layer graphene. This order is also observable in AFM topography and phase maps. AFM topography (Figure 4.7 a, c) provides consistent results with SEM observation (figure 4.7 e).

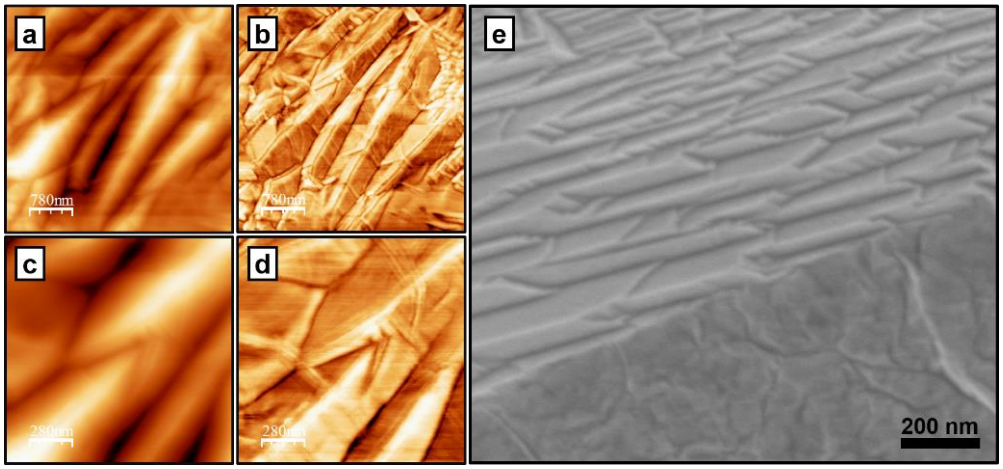

Figure 4.7 : (a, c) AFM topography and (b, d) corresponding phase maps of graphene/Cu sample. (e) SEM data shows single-multi layer graphene boundary. Crystallization of underlying copper surface can be seen in upper side of section (e).

Observing order of underlying copper substrate crystallization in partial grown graphene/Cu system proves the protection of graphene from oxidizing. In Figure 4.8, AFM topography and phase maps of partial grown graphene are shown. No clear crystalline surface orientation of copper could be observed in the regions that not covered with graphene. However, presence of graphene protects copper surface from oxidizing.

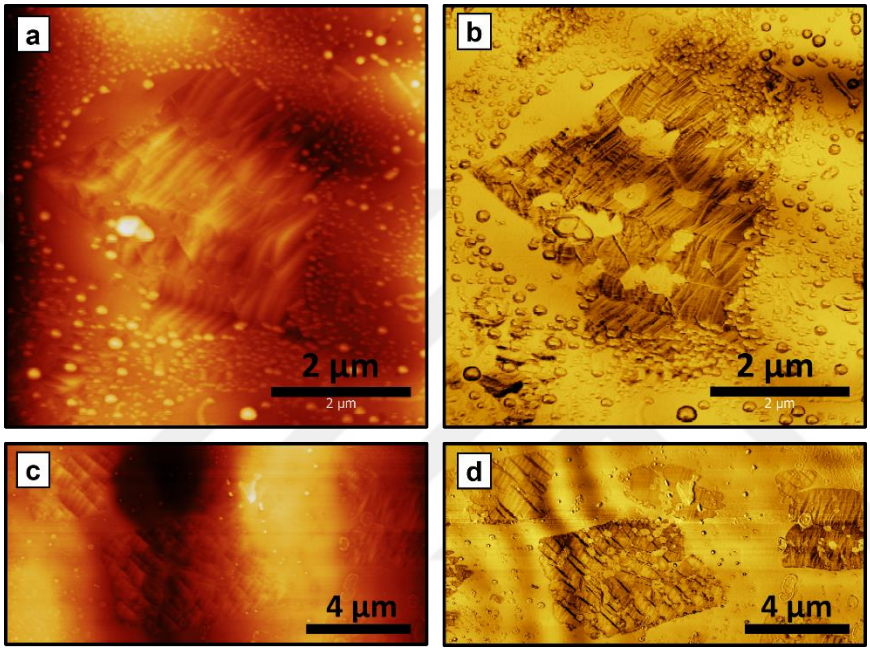

Figure 4.8 : (a, c) AFM topography and (b, d) corresponding phase maps of partial grown graphene/Cu sample. Partially growth of graphene is achieved by LP-CVD method.

5. CONTAMINATIONS AND DENDRITE FORMATION

5.1 Point-like Impurities and Fractal Contaminations

The most important result of this work in case of contribution to CVD grown graphene literature is the investigation of silicon-oxide contaminations on surfaces after CVD process and formation of such contaminations in dendritical shape. As mentioned in the literature review chapter of this thesis, silicon-oxide contaminations were observed before and reported in several studies but not discussed in detail [14-18]. We first observed tiny impurities on samples as other researchers [14-22] and investigated the reason of their existence. While we try to eliminate such impurities by varying CVD parameters, we discovered that it is possible to generate even larger silicon-oxide particles on the surface. As a result of our experiments, we produced large area point-like particles as well as particles in different dendritical shapes (Figure 5.1).

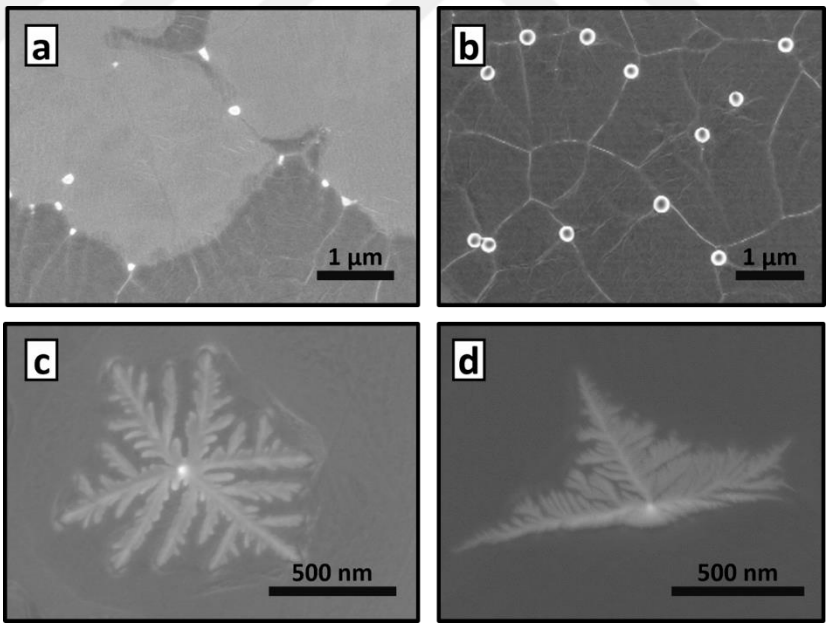

Figure 5.1: SEM images of different shape of silicon-oxide impurities observed on surface is shown. (a) Commonly encountered tiny impurities, (b) point-like particles and (c, d) different types of fractal formations due to contaminations on graphene/Cu sample. (V_{acc} = 2 kV for a,b, d and V_{acc} = 1.5 kV for c).

In fig 5.1, SEM images of four different types of silicon-oxide contaminations on different sample sets were shown. Figure 5.1 (a) shows commonly encountered tiny impurities on

graphene/Cu samples. Point-like particles (Figure 5.1 b) and different types of fractal formation of impurities (Figure 5.1 c, d) were obtained by varying CVD parameters. After observation of self-assembled silicon-oxide fractals on the surfaces, we aimed to investigate the formation mechanism of them.

5.2 Chemical Analysis

Previous studies about tiny impurities on graphene/Cu samples showed that they are made of silicon-oxide [ref]. In Figure 5.2, EDX measurement on a dendritic particle is given. While green spectrum was performed on the particle, the red one was performed on background graphene/Cu. Peaks corresponding to carbon and copper are common for both spectra as expected. However, green spectrum has additional peaks which, correspond to silicon and oxygen.

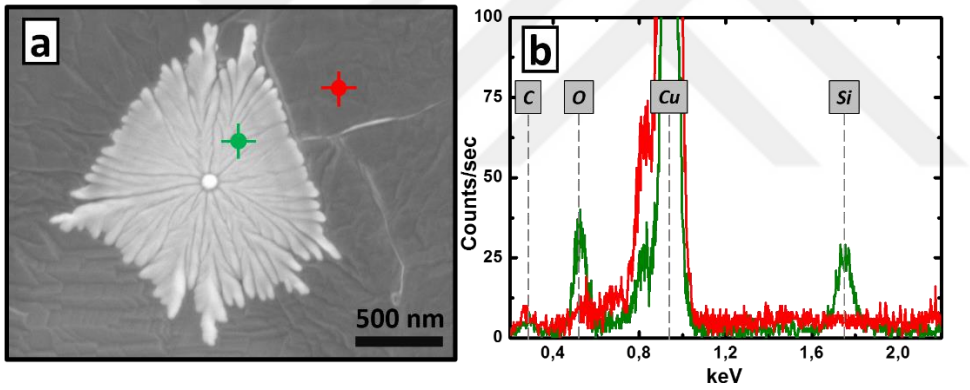

Figure 5.2 : EDX measurement on fractal impurity. (a) SEM image of particle and (b) corresponding EDX spectra (V_{acc} = 2 kV).

A possible explanation about the origin of silicon from previous studies is impurities in the bulk copper. This hypothesis is acceptable since observed silicon particles in these studies are tiny. However, in our case, number of contamination related spots and amount of silicon are higher. Small amount of impurity in bulk copper is not enough to supply such amount of silicon. Our idea about the origin of silicon is that, it may be originating from quartz, which is the only material including silicon in CVD chamber.

To show insufficiency of silicon impurities in copper bulk, we made calculation regarding the amount of silicon-oxide particles on sample. For this calculation, the sample set (S6) with homogeneous distribution of particles on surface was used. We calculated volumes

of particles on bare copper sample. To do that, static mode AFM measurements were performed and volume of single particle was calculated by Gwyddion software. According to results, volume of single particle is about $1.1x10^{-21}$ m^3. Since the particles are homogenously distributed on whole surface, we count the number of particles in unit area using SEM data (about 14 particles in 5 μm^2). According to our calculation, to obtain such amount of silicon-oxide particles on surface, it is needed that about 28 ppm silicon impurity should be in copper bulk [Appendix B]. However, from the product datasheet of our copper foils, amount of silicon impurities in the copper bulk is less than 2 ppm. Even if the whole impurity of 25 µm thick copper foil comes to the surface, it is clearly not enough to obtain such amount of particle on the surface. This calculation supports our idea that there should be another additional silicon source in the process.

A recent study about silicon contaminations in CVD-grown graphene mentioned the alpha-beta quartz phase transition happening at around 600 °C [22, 99]. Since the gas input and output regions of the quartz tube are at room temperature and the middle at 1000 °C, there is always a region that stays at around 600 °C and phase transition is continuously on-going. They suggested that due to the unstable phase transition caused by small variations in temperature during the growth process, silicon-oxide may get displaced and deposited on to copper foil [22].

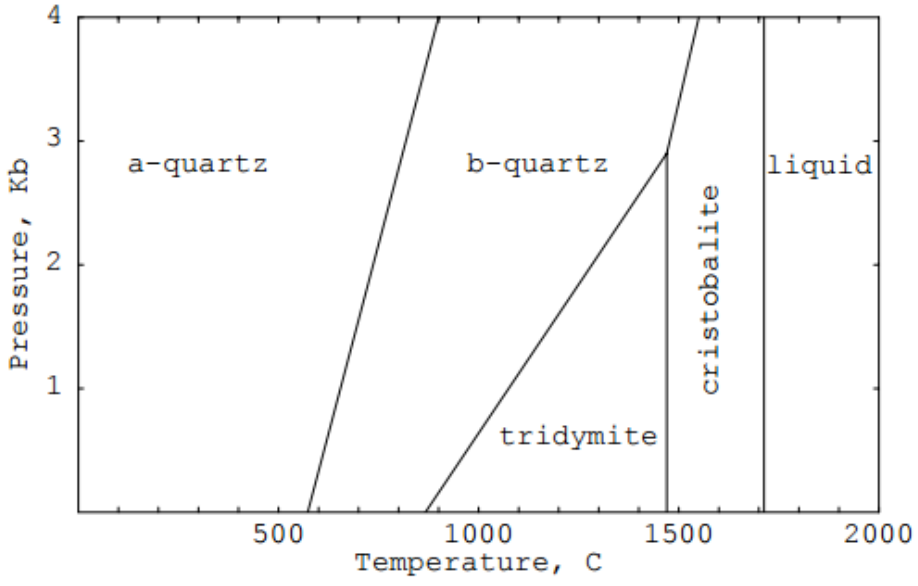

Figure 5.3 : The phase diagram of quartz [100].

The phase transition from α-quartz to β-quartz happens at 573°C in theory. Also, it is important to note that α-quartz has trigonal lattice and β-quartz has hexagonal lattice. [100, 99]. This phase transition is only based on changes in angles and lengths of chemical bonds, so atoms in quartz is just displaced slightly without breaking bonds. Because of that, such transition is called displacive. This change in crystal structure of quartz causes a change in the density also. Density of quartz changing from 2.65 g/cm^3 (α-quartz) to 2.53 g/cm^3 (β-quartz) [101].

Furthermore, another transition from β-quartz to tridymite phase, which happens at 870°C, requires breaking up and reconnection of chemical bonds. However, tridymite phase does not usually form from pure β-quartz. So, this transition is skipped generally and β-quartz transforms cristobalite directly at 1050°C [101].

Since the maximum temperature is 1000°C in the CVD growth process of graphene, cristobalite phase transition is not possible. However, as mentioned in literature review section, Wang et al. [21] showed that silicon-oxide particles occur on the copper surface when the temperature reached to around 850 °C in the CVD reactor. This temperature corresponds to reconstructive phase transition point from β-quartz to tridymite phase of quartz. According to our observations, increasing amount of silicon-oxide on the samples and obtaining large particles were achieved by increasing hydrogen concentration in the annealing atmosphere of CVD process. Generally skipped transition from β-quartz to tridymite phase may be happen under high hydrogen concentrated atmosphere and this may cause emanation of silicon from quartz. To approve the phase transition hypothesis as an explanation for silicon source, effect of hydrogen on reconstructive phase transition must be studied. On the other hand, rather than phase transition, etching phenomena and stealing silicon from quartz by annealing at around 1000 °C under highly hydrogen concentrated atmosphere must be studied also.

5.3 Effective Parameters on the formation of Impurities

After the first observation of tiny silicon impurities on samples, we worked on effective parameters which increase or decrease amount of contaminations on the surfaces. In this

respect, effect of hydrogen concentration in the annealing atmosphere, annealing time and amount of methane dosing on shape of particles were studied.

We have performed AP-CVD processes with different parameters. Depending on the growth parameters the shapes and sizes of such contaminants were observed to vary. Heating, annealing, during growth and cooling parameters for the AP-CVD processes are given in Table 5.1 with names of sample groups.

Table 5.1 : Table of growth conditions.

Sample Group	Heating & Annealing Atmos.(H_2 : Ar) [sccm]	Anneal time [min]	Growth Atmos. (H_2:Ar:CH_4) [sccm]	CH_4 Dosing time [min]	Cooling Atmos. (H_2:Ar) [sccm]	Shape of particles
S1	100:1000	60	100:1000:10	13	100:1000	Point
S2	100:1000	90	100:1000:10	5	100:1000	Point
S3	1000:1000	30	60:1000:5	3	60:1000	Point
S4	1000:1000	30	60:1000:10	3	60:1000	Dendritic
S5	1000:1000	30	60:1000:10	10	60:1000	Dendritic
S6	1000:1000	20	60:1000:0	0	60:1000	Flower

After the copper foils were heated under H_2 and Ar flow atmosphere up to the process temperature 1000 °C, the processes were performed by letting CH_4 into the chamber for the given periods. It took 140 min to reach to the process temperature of 1000 °C in all 6 processes. Later samples were cooled under H_2 and Ar flow atmosphere. For sample set 6 (S6) no CH_4 was used.

5.3.1 Hydrogen concentration and annealing time

The most representative results of the CVD processes are presented here. Parameters most effective on the number of impurities and the formation of dendrites were determined to be hydrogen flow during annealing, annealing time and the amount of methane dosing. Sample set S1 and S2 were annealed under 100 sccm hydrogen. In processes designated as S3, S4 and S5, the hydrogen concentration in the annealing atmosphere was 1000 sccm, but it was decreased to 60 sccm after annealing just before the start of the CH_4 dosing in order to obtain proper hydrogen concentration for graphene growth. To show the effect of

anneal time also, S1 was annealed for 60 minutes and S2 for 90 minutes using the same H_2 and Ar flow rates.

First, the effect of hydrogen flow rate in annealing atmosphere and annealing times were compared. Dependence of graphene growth on hydrogen flow was discussed before and increment of silicon-oxide impurities was observed as a function of H_2 amount used [20] but not mentioned. In Fig. 5.4, SEM images of samples from the processes S1, S2 and S4 were shown. Effect of hydrogen flow rate in the annealing atmosphere was observed to affect the number and shape of the silicon oxide nano particles significantly. In sample set S1 (Figure 5.4 a), hydrogen concentration in the annealing atmosphere was 100 sccm and annealing time was 60 minutes. We only observed tiny impurities on sample surface. However, when we increased annealing time to 90 minutes by keeping flowrate constant, it is observed that particles are bigger and shaped like flowers on surface (Figure 5.4 b). Furthermore, in sample set S4, hydrogen concentration in annealing atmosphere was increased to 1000 sccm. In figure 5.4 (c), resulting large dendritic particles were shown.

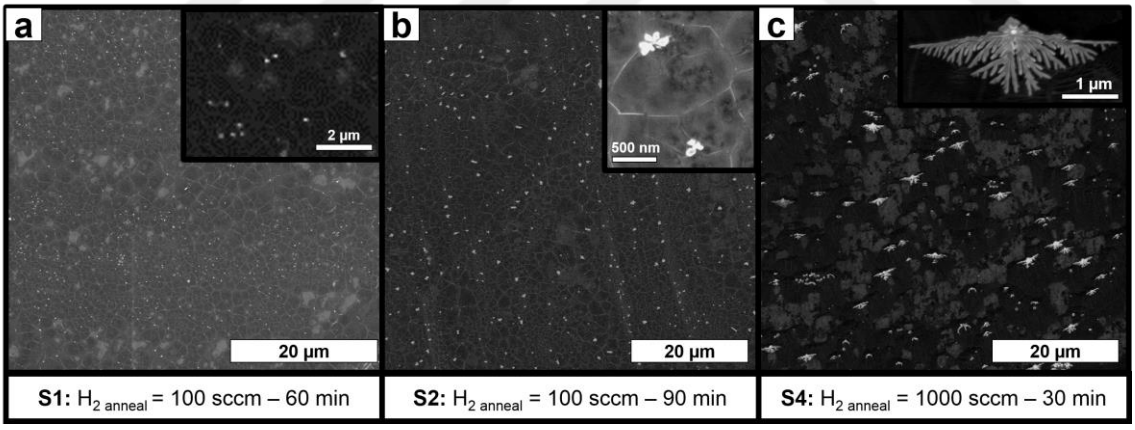

Figure 5.4 : Scanning electron micrographs of the processes (a) S1, (b) S2 and (c) S4 type growth of graphene. High H_2 flow rate results in the formation of dendritic structures rather than the point like contaminants (V_{acc} = 1.5 kV for a, b and V_{acc} = 2 kV for c).

5.3.2 Methane concentration and graphene growth

Although hydrogen concentration and annealing time increase amount of silicon on the surface, we figured out that there is not any fractal formation in the sample set named S3 (Figure 5.5 a). Comparison of the sample sets S3 and S4 in Figure 5.5 clearly shows that annealing under high hydrogen concentrated atmosphere is not enough to obtain dendritic

silicon-oxide on the surface. Despite the similar annealing conditions, which was supposed to result in the same amount of stolen silicon form the quartz tube, shapes of dendrites were observed to vary apparently due to the methane dosing. In order to check further the effect of methane, we prepared sample set S5 with longer CH_4 dosing time compared to S3 and S4. SEM images of these experiments according to methane dosing were shown in Figure 5.5.

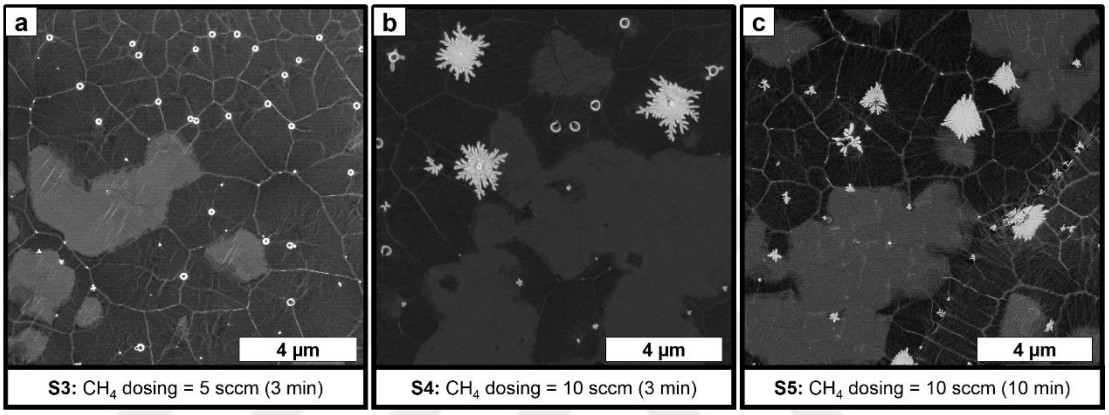

Figure 5.5 : Scanning Electron Micrographs of (a) S3, (b) S4 and (c) S5 type growth of graphene. (a) Point-like impurities and (b, c) different fractal formation of contaminations is shown according to methane dosing parameter. (V_{acc} = 2 kV for all SEM images)

Silicon impurities on sample S3 were point-like (Figure 5.5 a). When flow-rate of methane was doubled, dendrites occurred on surface (Figure 5.5 b, process S4). As we increased methane, shapes of dendrites changed (Figure 5.5 c, process S5). We have to note that point-like impurities on all samples can still be observed.

Since it is known that silicon impurities occur on copper surface before methane dosing and they are quite mobile [21], formation of graphene under such particles can affect their mobility. This fact may cause the dendritic formation of silicon. Since flow rate and exposure time of methane affect the graphene quality and number of layers in AP-CVD significantly [32], we observed changes in shapes of dendrites while changing methane dosing. Furthermore, on same sample, shapes of dendrites were observed to vary. SEM images of different regions of sample S4 were shown in both Figure 5.4 (c) and Figure 5.5 (b). They have deltoid geometry in Figure 5.4 (c) but hexagonal geometry in Figure 5.5 (b). We know that annealing polycrystalline copper helps to rearrange surface and cause

large copper grains with different local surface orientation. Since graphene growth on copper is strongly influenced by substrate surface orientations [102], dendrites can be shaped differently on the same sample according to graphene formation. Thus, substrate quality as well as the graphene-substrate combination may affect the general structure of the dendrites.

The formation of dendrites is apparently triggered by the altered mobility of the contaminant species on the surface. This becomes clearer upon comparing the processes of S3 and S4, which were almost the same. So, similar amount of silicon must be stolen from quartz reactor but the small amount of additional CH_4 triggers the formation of fractals.

Also the effect of the H coming from the CH_4 during the dehydrogenation process may be effective in the disturbance of the formerly generated silicon oxide clusters and their redistribution on the surface, by means of which these dendrites form. Keeping all the parameters the same and letting more CH_4 with an extended dosing time helped the fractals to grow even larger. This growth can also be due to the increase of the silicon species on the surface due to the H coming from CH_4. Yet the main effect seems to be the prolonged surface activity of the silicon species. On the other hand, comparison of S1 and S4 in Figure 5.4, shows that silicon occurs on the surface mainly due to H_2, and the H coming from CH_4 is not enough to generate additional silicon species on the surface. On S1, which is the one with the highest CH_4 dosing in all sample sets, we just observed tiny point like impurities (Figure 5.4 a). However, increasing anneal time in set S2, with less CH_4 dosing, caused a large amount of increase in silicon on surface when comparing the S1 (Figure 5.4 b). Thus, we state that the main reason of increasing silicon amount on the surface is hydrogen concentration.

In order to control the effect of the graphene formation on the growth of the dendrites we performed several CVD processes. Here process named S6 is exemplified during which no CH_4 was used. The same parameters with process S3 were used and we observed the formation of flower like shapes on bare copper foils (Figure 5.6), rather than point like silicon oxide clusters as in process S3. We also observed that grain boundaries of copper were filled with silicon-oxide. This process shows that the bulk of the silicon-oxide

originates during the heating up and annealing process and the shape and size distribution of the structures are governed by the CH_4 dosing, which is the graphene generation step. Such data support that, as the graphene changes the mobility of the particles on the surface, their final shapes were defined by the substrate.

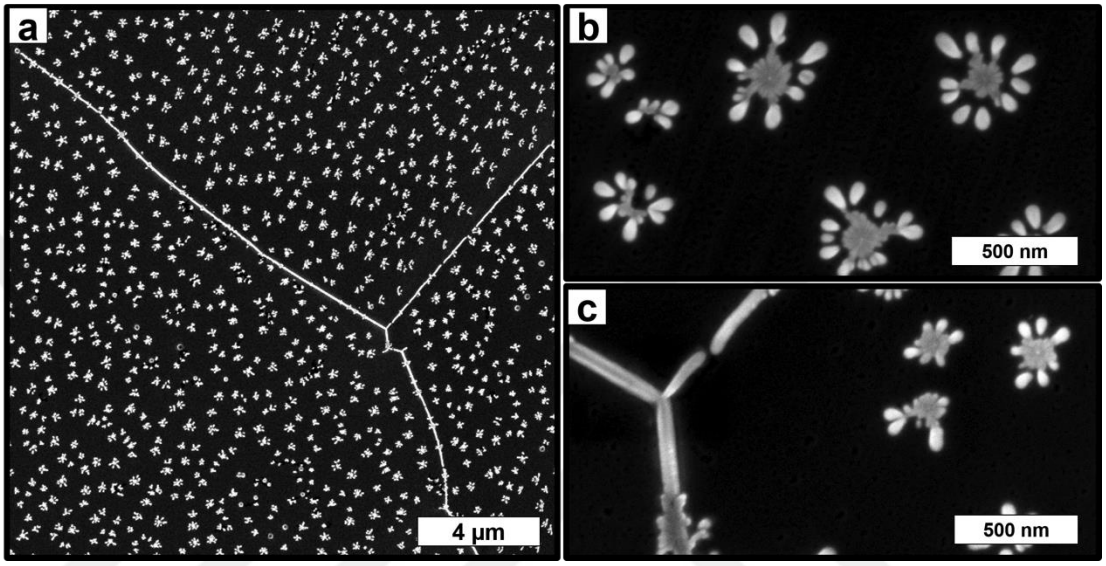

Figure 5.6 : Scanning Electron Micrographs of S6 type CVD process. (a) Large area image shows flower-like patterns formed by silicon-oxide particles. (b) and (c) are zoomed image on particles and filled grain boundaries (V_{acc} = 2 kV for all SEM images).

The most important observation here is the formation of distributed shapes rather than the point like clusters in the presence of graphene. It seemed that graphene may also cause the confinement of the silicon oxide clusters, and after some point, fractals were allowed as seen in the comparison of processes S3 and S6. The nucleation of the second layer may be releasing some tension at the graphene-Cu interface there by making the silicon species more diffusive on the surface. These hypotheses must certainly be further tested.

In order to check if the silicon oxide distribution on the surface is a function of the heights of these structures, we performed atomic force microscopy measurements on the samples. Topography maps and height profiles of different types of silicon-oxide impurities are shown in Figure 5.7. Point-like impurities on graphene from sample set S3, which have heights about 200 nm, are much higher than both dendritic ones and ones on copper. However, they are quite small in lateral direction according to others. Also note that point-like particles were confined to the grain boundaries (Figure 5.7 d).

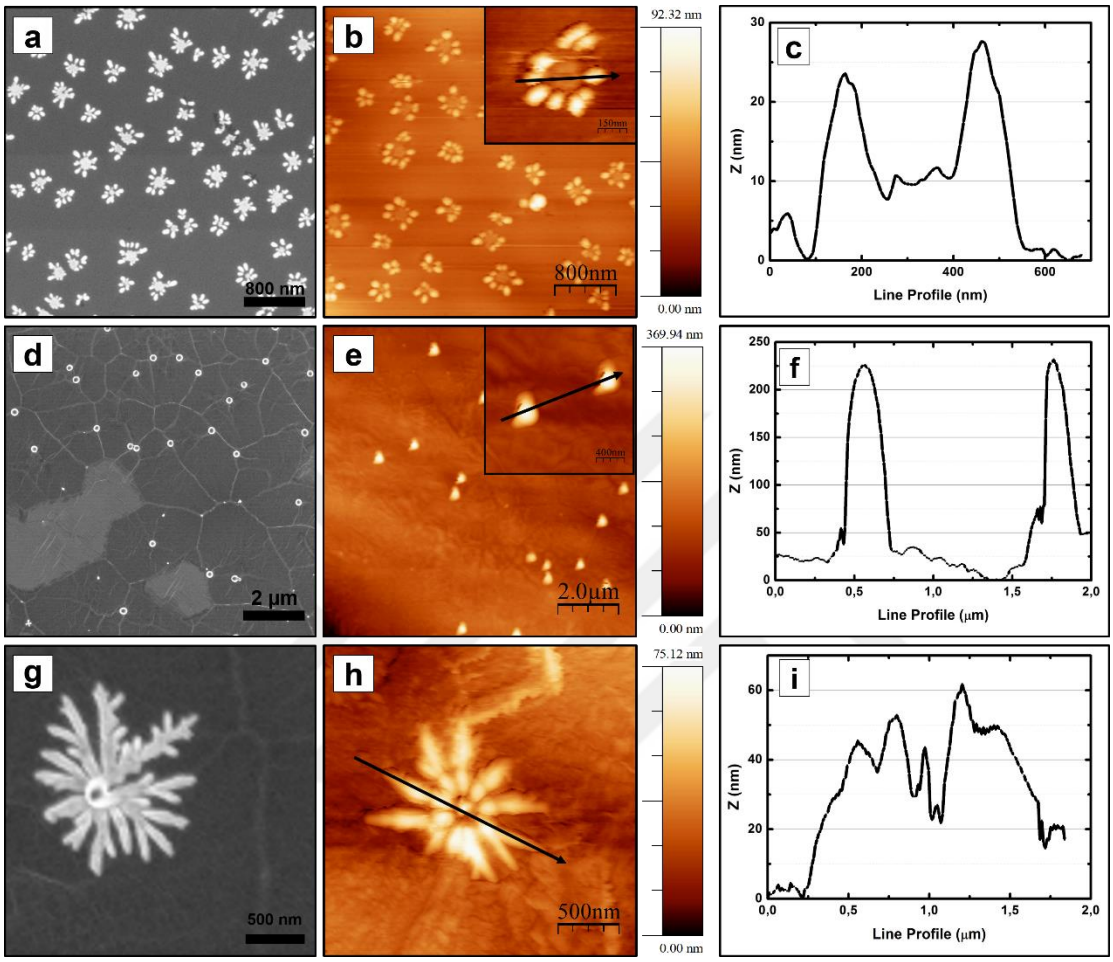

Figure 5.7 : Each row correspond different samples set (a: S6, d: S3, g: S4). (a,d,c) SEM images of different types of silicon-oxide and (b,e,h) static-mode AFM topography maps. (c,d,i) Line profiles of dendrites.

Since the annealing conditions are the same for the sets from S3 to S6, total amount of silicon species on the surfaces should be equal. To check this we calculated total volume of silicon-oxide particles on 4 µm by 4 µm scanning regions. In figure 5.8, AFM topographies and total volume of particles on the maps are shown. According to the calculations, total volume of particles are close to each other which support the idea of bulk amount of silicon on samples were caused by high hydrogen annealing and methane dosing, or graphene formation, affects the distribution and shapes of particles. However, since the particle distribution is not homogeneous on sample sets S3 and S4, it is needed to perform lots of measurements and proper averaging to make appropriate comparison.

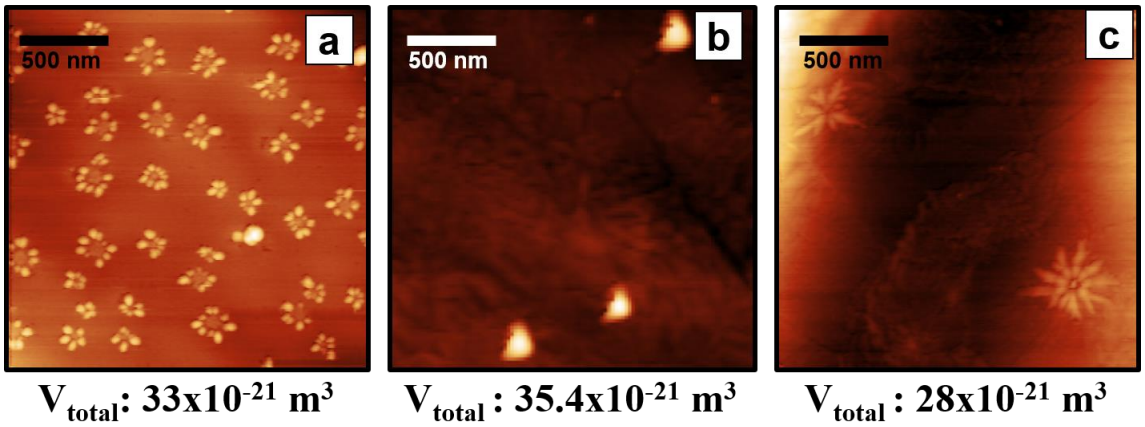

Figure 5.8: AFM topography maps of samples from sets (a) S6, (b) S3 and (c) S4. Total volumes of silicon-oxide particles on the scanning regions are written under each map. All scanning areas are 4 µm by 4 µm.

5.3.3 Further observations

Besides the investigation about formation mechanism of dendrites, in order to check if we could manipulate the silicon-oxide structures, we tried to etch them by O_3 under the e-beam of the Scanning Electron Microscope. One experiment is shown in Figure 5.9. It is possible to etch such dendrites by ozone and create a cloud of silicon-oxide nano particles around it while keeping the general structure of the dendrite.

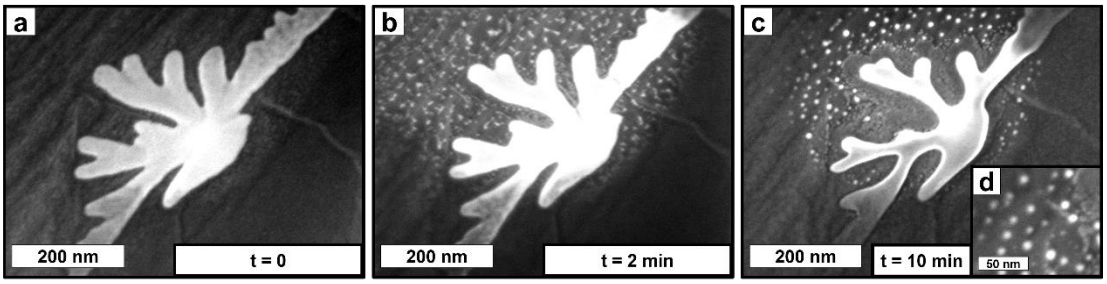

Figure 5.9 : Scanning Electron Micrographs of etching time lapse. SEM image of (a) before, after (b) 2 and (c) 10 minute etching is shown. (d) Zoomed image of nano particles which were created by etching (V_{acc} = 20 kV for all SEM images).

Moreover, silicon-oxide particles on both graphene/Cu and bare Cu surface can be transferred on to arbitrary substrates by using same procedure of PMMA-based wet transfer method of graphene [92]. Examples of transferred particles on SiO_2 wafer is shown in Figure 5.10. Since nano-scale particles on bare copper surface are

homogeneously distributed on the whole surface, this could be a new method to produce silicon-oxide nanoparticles.

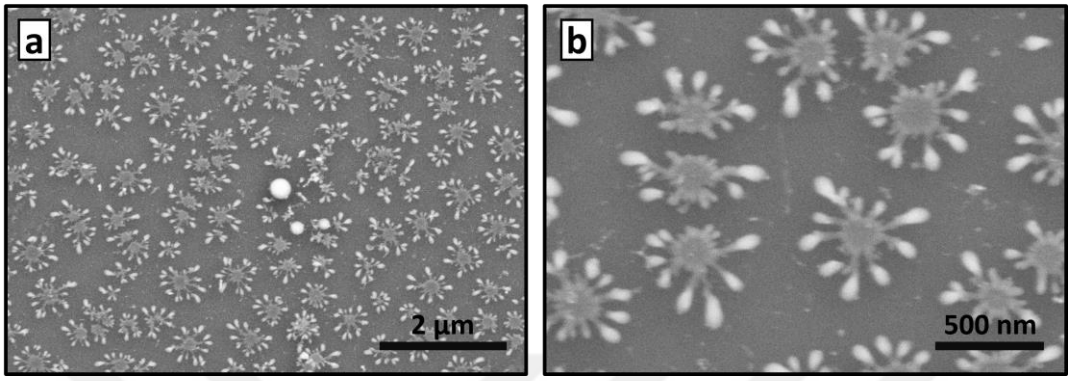

Figure 5.10 : (a, b) Scanning Electron Micrographs of transferred silicon-oxide particles on SiO_2 wafer. Homogeneously distribution of particles on whole surface can be seen (V_{acc} = 5 kV for all SEM images).

5.4 Lateral Force Microscopy Study on Dendrites

As mentioned in the previous chapter, It must be checked that whether such particles stay on top of the graphene or at the interface of graphene and copper. To clarify the location of particles in the presence of graphene, we used Lateral Force Microscopy. Basically, we aimed to check if particles are covered by graphene or not. Since we have silicon-oxide particles without any graphene formation on bare copper surface (S6), we aimed to measure friction of bare silicon-oxide particles as a reference and then decide if dendritic particles are covered with graphene by comparing with reference measurement. First, friction measurements were performed on bare silicon-oxide particles with the method explained in section 2.3.4. Results of the experiments are shown in Figure 5.11. Load force and scanning velocities were varied due to the direct effects on friction force [103]. The graphic in figure 5.11 (d) shows friction measurements as a function of load force with different scanning speeds. For every measurement set with certain speed, overall friction coefficient (µ) is written on graph. Since the friction force is changing according to load force and scanning speed, we kept these parameters constant for all measurements from different sample sets. AFM topography and simultaneously recorded friction map of sample from set S6 are shown in Figure 5.11 (b) and (c). It is important to mention that friction maps were obtained by eliminating morphological effects (with the method which

explained in Section 2.3.4) and only shows difference in friction coefficient of surface. The graphic in Figure 5.11 (e) shows force distribution on friction map in Figure 5.11 (c). According to histogram, average friction force between particles and tip were measured to be around 10-12 nN, while the friction between the tip and copper surface is around 6,5 nN. We consider this force range of 10-12 nN as our reference for LFM measurements on particles with the presence of graphene on the surface.

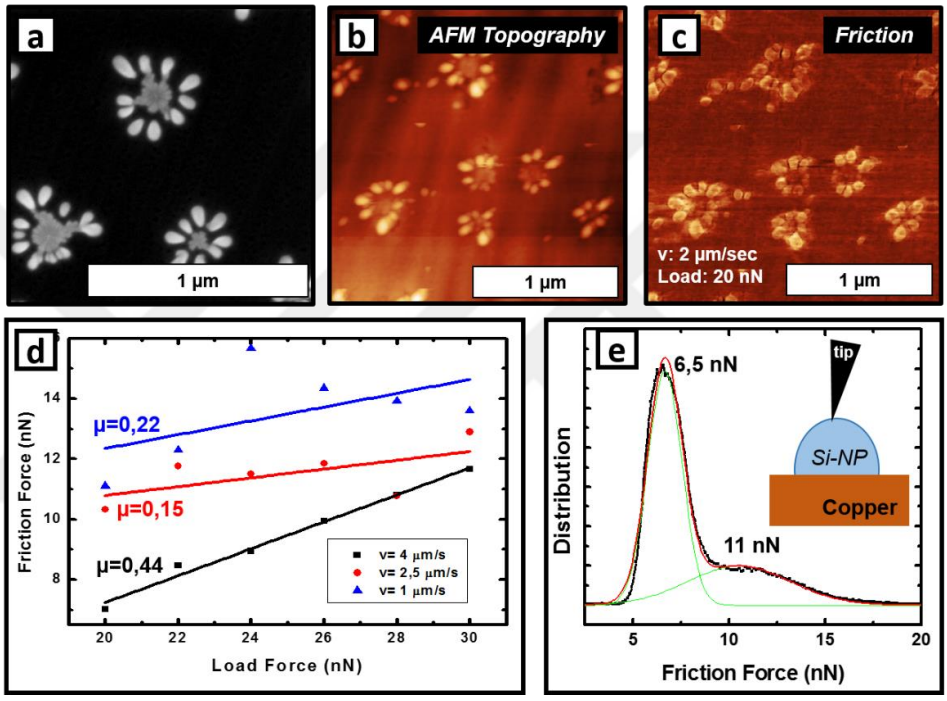

Figure 5.11 : (a) SEM image of silicon-oxide particles on Cu surface. (b) AFM topography map and (c) corresponding friction force map of surface. (d) Experiments performed by varying scanning parameters; load force and scanning speed. (e) Histogram analysis of friction force map in section (c) showing measured friction forces on particles and background copper substrate.

After the reference measurement on bare particles on Cu foil, by keeping scanning parameters constant, we performed LFM measurements on samples with the presence of graphene and measured friction forces on the particles. Results of measurements on three different types of silicon-oxide particles are shown in Figure 5.12.

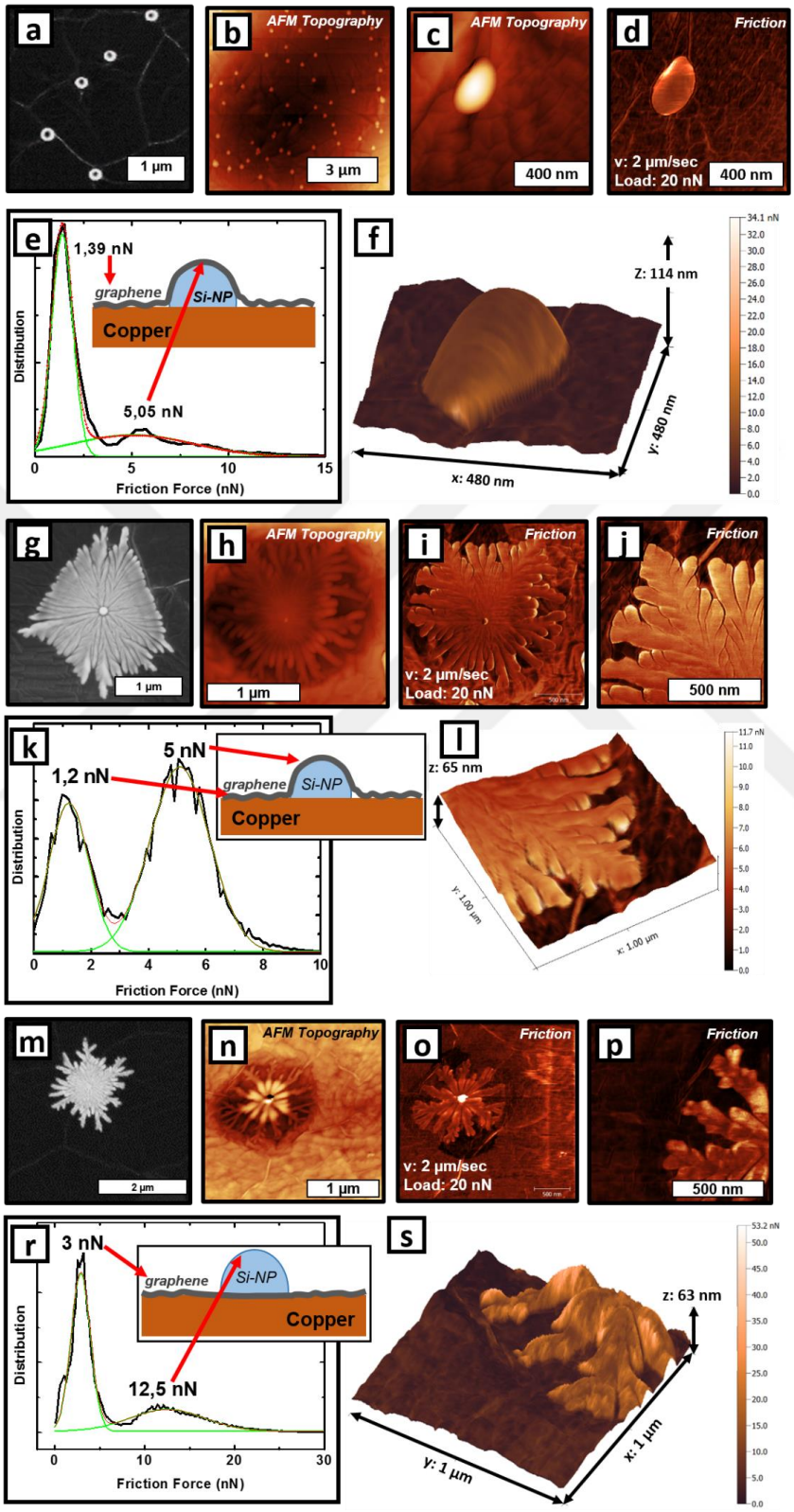

Figure 5.12 : (a, g, m) SEM image of different type of impurities on graphene/Cu samples. (c, h, n) AFM topography maps and (d, i, o) corresponding friction force maps

Figure 5.12 (continued) : of surface. (e, k, r) Histogram analysis graphics of friction force maps of (d, j, p) showing measured friction forces on particles and background copper substrate. (f, l, s) are 3D maps of regions (c, i, o), achieved by overlaying (d, j, p) on topography maps. xyz-scales shows topography while color scale shows friction force.

Measurements on point-like silicon-oxide particles resulted that friction on particles was measured to be around 5.5 nN, which is almost half of the reference value (Figure 5.12 e). Also, friction on fractal particle in Figure 5.12 (g) was measured as in the same range. Since friction on two different particle types were measured in the same range and it is not close to the reference value, we conclude that such particles may be covered with graphene. However, friction measurements on another type of fractal (Figure 5.12 m) was measured to be 12.5 nN, like our reference measurement. So, we conclude that this fractal are not covered with graphene.

On the other hand, friction measurements for background graphene/copper sample resulted in different values. In the Figure 5.12 (e and k) measured frictions on graphene are in the range of 1.2-1.4 nN, while in Figure 5.12 (r) it is 3 nN. Previous friction study on CVD-grown graphene on copper showed that friction of graphene is strongly dependent on substrate and measured friction is around 2 nN on bilayer graphene while it is around 3 nN on single-layer graphene with 20 nN load force [104]. Therefore, we predict that particles in the Figure 5.12 (e and k) are on bilayer graphene, while particle in Figure 5.12 (r) is on single-layer graphene.

According to characterization regarding friction properties of particles, point-like silicon-oxide particles were determined to be at graphene-Cu interface (Figure 5.12 a-f). Measurements on fractal particles resulted that fractals are covered with graphene, if they are on bilayer graphene region (Figure 5.12 g-l). However, some fractal formations were measured not to be covered with graphene if they stay at single layer graphene region (Figure 5.12 m-s).

5.5 Hypothesis on Fractal Formation

First of all, effective parameters on formation of fractals on samples were studied. Fractal formation is triggered with methane dosing. Since it directly affects the formation of graphene and changes growth dynamics, we can safely claim that agglomeration of

silicon-oxide clusters on surface is strongly affected by existence of graphene and number of layers. Moreover, this was proved by a CVD process (sample set: S6) without methane exposure. In this sample set, we observed flower-like particles on bare copper surface. However, with the presence of graphene, particle shapes are varying from dot-like particles to different fractal formations depending on methane dosing.

On the other hand, on different spots of same sample, it is also possible to observe different types of fractals (Sample set: S4, Figure 5.4 c and Figure 5.5 b). For this observation, we refer to polycrystalline nature of copper substrate and dependency of graphene growth dynamics on copper surface orientation. Since surface crystalline differently after high temperature annealing, growth dynamics of graphene is varying on surface according to surface orientation [102]. Varying growth of graphene on surface affects the formation of fractals and result in varying types of fractal formation on same sample.

Friction force measurements revealed that particles could be covered with graphene in multilayer grown regions and not covered in single layer areas. According to this observation, we can speculate that agglomeration of silicon-oxide on surface happen at graphene-Cu interface. After the graphene growth is completed and CVD chamber start to cool down, graphene on particle may be ripped due to the additional tension caused by underlying particle. However, if graphene on cluster is multilayered, tension relief may not be able to rip graphene. In that case, formation of fractal happens under the graphene.

6. CONCLUSION AND OUTLOOK

We focused on growing graphene by Chemical Vapor Deposition method on polycrystalline copper foils. A new CVD setup was built which is suitable for both atmospheric and low-pressure conditions for the purpose of the graphene production. Both full as well as partial coverage of single and multi-layer graphene were grown on copper samples. Raman spectroscopy was performed on samples in order to determine number of graphene layer. For the investigation on morphological and electronical properties of graphene, Scanning Tunneling Microscopy and Atomic Force Microscopy measurements were performed under ambient conditions. Atomic scale characterization of graphene on copper samples by STM resulted in observation of honeycomb lattice of graphene as well as surface orientation of underlying copper substrate. Continuity and behaviour of graphene layer on the step-edges of copper were investigated. Moiré patterns were observed on surfaces providing information about the interaction between graphene and copper.

On the other hand, during our study on optimizing CVD process, we encountered some droplet like impurities on surfaces. Such contaminations on CVD-grown graphene surfaces are commonly encountered silicon-oxide particles, generally believed to originate from quartz or impurities in bulk copper foil. We discovered that it is possible to obtain even larger silicon-oxide particles on samples. As a result of many experiments, we developed a methodology to produce different shapes and sizes of particles on surfaces. Moreover, we observed fractal formation of such contaminations on surfaces. The important parameters were determined to be hydrogen concentration in annealing atmosphere, annealing time and amount of methane dosing. Hydrogen in annealing atmosphere is responsible for bulk amount of silicon from quartz. Final shapes of clusters were governed by methane dosing, which directly affect the graphene formation on surface. Therefore, it can be safely claimed that presence of graphene has an influence on particle shapes and fractal formations. Furthermore, we also produced homogeneously distributed nano-scale silicon-oxide particles on bare Cu foil. Since such particles can be transferred on to arbitrary substrate by using same procedure with similar to graphene

transfer, this can be presented as a new and relatively easy method for production of silicon-oxide nanoparticle production and deposition.

As a part of this study on the formation mechanism of fractal structures, we aimed to determine whether particles were located at the graphene-Cu boundary or on the graphene layer, since the shapes are determined by graphene formation. For that purpose, we used Lateral force Microscopy, which is a method for measuring friction force between tip and surface by using the torsional cantilever bending. According to our measurements, point-like confined particles stay at the graphene-Cu boundary. Fractal particles in multilayer graphene region were measured to be covered with graphene as well. However, some fractal particles are not covered with graphene if they are in single layer graphene region. The hypothesis about the formation mechanism of fractal structures were suggested as happening at the graphene-copper interface.

REFERENCES

[1] **Kroto, H. W., et al.** (1985). C60: Buckminsterfullerene. *Nature,* 318, 162-163.

[2] **Bethune, D. S., et al**. (1993). Cobalt-catalysed growth of carbon nanotubes with single atomic-layer walls. *Nature* 363, 605-607.

[3] **Iijima, S. and Ichihashi, T.** (1993). Single-shell carbon nanotubes of 1-nm diameter. *Nature,* 363, 603-605.

[4] **Wallace, P. R.** (1947). The Band Structure of Graphite. *Physical Review,* 71, 622-634.

[5] **Boehm, H. P., Setton, R. and Stumpp, E.** (1994). Nomenclature and terminology of graphite intercalation compunds. *Pure Appl. Chem.,* 66, 9, 1893-1901.

[6] **Castro, A. H., et al.** (2009). The electronic properties of graphene. *Rev. Mod. Phys.,* 81, 109.

[7] **Chen, J., et al.** (2008). Intrinsic and extrinsic performance limits of graphene devices on SiO_2. *Nature Nanotechnology,* 3, 206-209.

[8] **Du, X., et al.** (2009). Fractional quantum Hall effect and insulating phase of Dirac electrons in graphene. *Nature,* 462, 192-195.

[9] **Wu, X., et al.** (2009). Half integer quantum Hall effect in high mobility single layer epitaxial graphene. *Appl. Phys. Lett.,* 95, 223108.

[10] **Nair, R. R., et al.** (2008). Fine Structure Constant Defines Visual Transparency of Graphene. *Science,* 320, 5881, 1308.

[11**] Novoselov, K. S., Geim, A. K. and Morozov, S.V.** (2004). Electric field effect in atomically thin carbon films. *Science*, 306, 5696, 666-669.

[12] **Novoselov, K. S., et al.** Two-dimensional gas of massless Dirac fermions in graphene. *Nature,* 438, 197-200.

[13] **The Nobel Prize in Physics 2010.** (2010, October 5). Retrieved from http://www.nobelprize.org/nobel_prizes/physics/laureates/2010/.

[14] **Li, X., et al.** (2009). Large-area synthesis of high-quality and uniform graphene films on copper foils. *Science,* 324, 1312.

[15] **Rasool, H. I., et al.** (2011). Atomic-Scale Characterization of Graphene Grown on Copper (100) Single Crystals. *J. Am. Chem. Soc.,* 133, 12536-12543.

[16] **Wu, B., et al.** (2011). Equiangular Hexagon-Shape-Controlled Synthesis of Graphene on Copper Surface. *Adv. Mater.,* 23, 3522-3525.

[17] **Kim, H., et al.** (2012). Activation Energy Paths for Graphene Nucleation and Growth on Cu. *ACS Nano,* 6, 4, 3614-3623.

[18] **Safron, N. S. and Arnold, M. S.** (2014). Experimentally determined model of atmospheric pressure CVD of graphene on Cu. *J. Mater. Chem. C,* 2, 744.

[19] **Rasool. H. I., et al.** (2010). Continuity of Graphene on Polycrystalline Copper. *Nano Lett.*, 11, 1, 251-256.

[20] **Jacobberger, R. M. and Arnold, M. S.** (2013). Graphene Growth Dynamics on Epitaxial Copper Thin Films. *Chem. Mater.*, 25, 871-877.

[21] **Wang, Z., et al.** (2015). Direct Observation of Graphene Growth and Associated Copper Substrate Dynamics by in Situ Scanning Electron Microscopy. *ACS Nano*, 9, 2, 1506-1519.

[22] **Ruiz, I., et al.** (2014). Silicon Oxide Contamination of Graphene Sheets Synthesized on Copper Substrates via Chemical Vapor Deposition. *Adv. Sci. Eng. Med*, 6, 1-6.

[23] **Mattevi, C., et al.** (2011). A review of chemical vapour deposition of graphene on copper. *J. Mater. Chem.*, 21, 3324-3334.

[24] **Banerjee, B. C., Hirt, T. J. and Walker Jun, P. L.** (1961). Pyrolytic Carbon Formation from Carbon Suboxide. *Nature*, 192, 450-451.

[25] **Acheson, E. G.** (1896). *United States Patent* No. 568,323.

[26] **Arsem, W. C.** (1911). Transformation of Other Forms of Carbon into Graphite. *Ind. Eng. Chem.*, 3, 799, 799-804.

[27] **Karu, A. E. and Beer M. J.** (1966). Pyrolytic Formation of Highly Crystalline Graphite Films. *J. Appl. Phys.*, 37, 2179.

[28] **Morgan, A. E. and Samorjai, G. A.** (1968). Low energy electron diffraction studies of gas adsorption on the platinum (100) single crystal surface. *Surf. Sci.*, 12, 405.

[29] **Hagstrom, S., Lyon H. B. and Somorjai, G. A.** (1965). Surface Structures on the Clean Platinum (100) Surface. *Phys. Rev. Lett.*, 15, 491.

[30] **Ong, T. P., et al.** (1992). Nucleation and growth of diamond on carbon-implanted single crystal copper surfaces. (1992). *J. Mater. Res.*, 7, 2429-2439.

[31] **Lee, S. T., et al.** (1991). Heteroepitaxy of carbon on copper by high-temperature ion implantation. *Appl. Phys. Lett.*, 59, 785.

[32] **Bhaviripudi, S., et al.** (2010). Role of Kinetic Factors in Chemical Vapor Deposition Synthesis of Uniform Large Area Graphene Using Copper. *Nano Lett.*, 10, 10, 4128-4133.

[33] **Celebi, K., et al.** (2013). Evolutionary Kinetics of Graphene Formation on Copper. *Nano Lett.*, 13, 3, 967-974.

[34] **Gardiner, D.J.** (1989). Practical Raman spectroscopy. *Springer-Verlag*. ISBN: 978-0-387-50254-0.

[35] **Schrader, B.** (1995). Infrared and Raman Spectroscopy. *VCH Publishers Inc.*, New York.

[36] **Malard, L.M., et al.** (2009). Raman Spectroscopy in Graphene. *Phys. Rep.*, 473,

5-6, 51-87.

[37] **Goldstein J., et al.** (2003). Scanning Electron Microscopy and X-ray Microanalysis, 3ed. *Luwer Academic/Plenum Publishers,* New York.

[38] **Russ, J. C.** (1984). Fundamentals of Energy Dispersive X-ray Analysis. *Butterworths.* London.

[39] **Reed S. J. B.** (2005). Electron Microprobe Analysis and Scanning Electron Microscopy in Geology. *Cambridge University Press*.

[40] **Agarwal, B. K.** (1991). X-ray Spectroscopy, 2nd ed. *Springer-verlag*. Berlin.

[41] **Knoll, M. an441d Ruska, E. Z.** (1932). Das Elektronenmikroskop. *Physik,* 78, 318.

[42] **Broglie, L. D.** (1925). *Ann. Phys. (Paris),* 3, 22.

[43] **Stokes D. J.** (2008). Principles and Practice of Variable Pressure, Environmental Scanning Electron Microscopy. *A John wiley and sons ltd.*

[44] **Scire, F., Ward, J. and Young, R.** (1972). The Topografiner: An Instrument for Measuring Surface Microtopography. *Rev. Sci. Ins.,* 43, 7.

[45] **Binnig, G. and Rohrer, H.** (1986). Scanning tunneling microscopy. *IBM Journal of Research and Development,* 30, 4, 355.

[46] **The Nobel Prize in Physics 1986.** (1986, October 15). Retrieved from http://www.nobelprize.org/nobel_prizes/physics/laureates/1986/.

[47] **Schrödinger, E.** (1926). An Undulatory Theory of the Mechanics of Atoms and Molecules. *Phys. Rev.,* 28, 1049.

[48] **Chen, C. J.** (1993). Introduction to Scanning Tunneling Microscopy. *New York: Oxford University Press*.

[49] **Binnig, G., et al.** (1983). 7 × 7 Reconstruction on Si(111) Resolved in Real Space. *Phys. Rev. Lett.,* 50, 120.

[50] **Binnig, G., Quate, C. F. and Gerber, C.** (1986). Atomic Force Microscopy. *Phys. Rev. Lett.,* 56, 930.

[51] **Demtröder, W.** (2005). Molecular Physics. *Wiley-VCH,* Germany, 116-118.

[52**] Hirschfelder J.O.** (1967). Intermolecular Forces. *Wiley-VCH*, New York.

[53] **Atkins, P. and Julio, P.** (2006). Physical Chemistry for the Life Sciences. *N.Y.W.H. Freeman Company.* New York, 469-472.

[54] **Garcia, R. and Perez, R.** (2002). Dynamic atomic force microscopy methods. *Surface Science Reports,* 47, 197-301.

[55] **French, A. P.** (1971). Vibration and Waves, The MIT Introductory Physics Series. *WW. Norton and Co,* New York.

[56] **Paulo, A. S. and Garcia, R.** (2001). Tip-surface forces, amplitude, and energy dissipation in amplitude-modulation (tapping mode) force microscopy. *Phys. Rev. B,* 64, 1934.

[57] **Carpick, R. W. and Salmeron, M.** (1997). Scratching the Surface: Fundamental Investigations of Tribology with Atomic Force Microscopy. *Chem. Rev.*, 97, 1163.

[58] **Gnecco, E., et al.** (2003). Friction and wear on the atomic scale. *Wear*, 254, 859.

[59] **Mate, C. M., et al.** (1987). Atomic-scale friction of a tungsten tip on a graphite surface. *Phys. Rev. Lett.*, 59, 1942.

[60] **Wenhua, L., Keith, B. and Guthold, M.** (2007). Easy and direct method for calibrating atomic force microscopy lateral force measurements. *Rev Sci Instrum.*, 78, 6.

[61] **Nano Sensors Product Catalogue.** http://www.nanosensors.com/PointProbe-Plus-Contact-Mode-Short-Cantilever-Reflex-Coating-afm-tip-PPP-CONTSCR.

[62] **Liu, W., et al.** (2011). Synthesis of high-quality monolayer and bilayer graphene on copper using chemical vapor deposition. *Carbon*, 49, 4122-4130.

[63] **Earnshaw, A. and Harrington, T. J.** (1972). The chemistry of the transition elements. *Oxford University Press*.

[64] **Oshima, C. and Nagashima, A.** (1997). Ultra-thin epitaxial films of graphite and hexagonal boron nitride on solid surfaces. *J. Phys. Condens. Matter*, 9, 1.

[65] **Sutter, P. W., Flege, J. I. and Sutter, E. A.** (2008). Epitaxial Graphene on Ruthenium. *Nat. Mater.*, 7, 406-411.

[66] **Himpsel, F.J., et al.** (1982). Adsorbate Band Dispersions for C on Ru(0001). *Surf. Sci.*, 115.

[67] **Coraux, J., et al.** (2008). Structural Coherency of Graphene on Ir(111). *Nano Lett.*, 8, 2, 565-570.

[68] **Kholin, A., et al.** (1985). *Sov. Phys. Solid State*, 27, 155.

[69] **Hamilton, J. C. and Blakely, J. M.** (1980). Surface Carbon Segregation in Dilute Alloys of Pt, Pd and Co. *Surface Science*, 91, 199.

[70] **Gall, N. R., et al.** (1985). *Sov. Phys.Solid State*, 27.

[71] **Eizenberg, M. and Blakely, J. M.** (1979). Carbon Monolayer Phase Condensation on Ni(111). *Surface Science*, 82, 1, 228-236.

[72] **Reina, A., et al.** (2009). Large Area, Few-Layer Graphene Films on Arbitrary Substrates by Chemical Vapor Deposition. *Nano Lett.*, 1, 30-35.

[73] **Ong, T. P., et al.** (1992). Nucleation and growth of diamond on carbon-implanted single crystal copper surfaces. (1992). *J. Mater. Res.*, 7, 2429-2439.

[74] **Constant, L., Speisser, C. and Le Normand, F.** (1997). HFCVD diamond growth on Cu(111). Evidence for carbon phase transformations by in situ AES and XPS. *Surface Science*, 387, 28-43.

[75] **Zhou, W., et al.** (2006). Copper Catalyzing Growth of Single-Walled Carbon Nanotubes on Substrates. *Nano Lett.*, 6, 12, 2987-2090.

[76] **Ding, L., et al.** (2009). Selective Growth of Well-Aligned Semiconducting Single-Walled Carbon Nanotubes. *Nano Lett.*, 9, 800-805.

[77] **Lee, S. T., et al.** (1991). Heteroepitaxy of Carbon on Copper by High-Temperature ion-implantation. *Appl. Phys. Lett.*, 59, 785-787.

[78] **McLellan, R.** (1969). The solubility of carbon in solid gold, copper, and silver. *Scr. Metall.*, 3, 6, 389-391.

[79] **Lopez, G. A. and Mittemeijer, E. J.** (2004). The Solubility of C on Solid Cu. *Scr. Metall.*, 51, 1, 1-5.

[80] **Li, X., et al.** (2009). Evolution of Graphene Growth on Ni and Cu by Carbon Isotope Labeling. *Nano Lett.*, 9, 12, 4268-4272.

[81] **Earnshaw, A. and Harrington, T. J.** (1972). The chemistry of the transition elements. *Oxford University Press*.

[82] **Sutter, E., Albrecht, P. and Sutter, P.** (2009). Graphene growth on pollycrystalline Ru thin films. *Appl. Phys. Lett.*, 95, 133109.

[83] **Kim, H., et al.** (2013). Modeling of the self-limited growth in catalytic

chemical vapor deposition of graphene. *New Journal of Physics*, 15, 053012.

[84] **Zhang, W., et al.** (2011). First-principles thermodynamics of graphene growth on Cu surfaces. *J. Phys. Chem. C*, 115, 17782-17787.

[85] **Van Wesep, R., et al.** (2011). Communication: Stable Carbon Nanoarches in the Initial Stages of Epitaxial Growth of Graphene on Cu(111). *J. Chem. Phys.*, 134, 171105.

[86] **Wu, P., et al.** (2010). Communication: Coalescence of Carbon Atoms on Cu (111) Surface: Emergence of a Stable Bridging-Metal Structure Motif. *J. Chem. Phys.*, 133, 071101.

[87] **Vlassiouk, I., et al.** (2011). Role of Hydrogen in Chemical Vapor Deposition Growth of Large Single- Crystal Graphene. *ACS Nano*, 5, 7, 6069-6076.

[88] **Galea, N. M., Knapp, D. and Ziegler, T.** (2007). Density Functional Theory Studies of Methane Dissociation on Anode Catalysts in Solid-Oxide Fuel Cells: Suggestions for Coke Reduction. *J. Catal.*, 247, 20-33.

[89] **Gao, L., et al.** (2010). Efficient Growth of High-Quality Graphene Films on Cu Foils by Ambient Pressure Chemical Vapor Deposition. *Appl. Phys. Lett.*, 2010, 97, 183109–183111.

[90] **Vlassiouk, I., et al.** (2013). Graphene Nucleation Density on Copper: Fundamental Role of Background Pressure. *J. Phys. Chem. C*, 117, 37, 18919-18926.

[91] **Fonda, G.R.** (1928). Evaporation of tungsten under various pressure of argon. *Phys. Rev.*, 31, 260.

[92] **Liang, X., et al.** (2011). Toward Clean and Crackless Transfer of Graphene. *ACS Nano*, 5, 11, 9144-9153.

[93] **Ferrari, A.C., et al.** (2006). Raman Spectrum of Graphene and Graphene Layers. *Phys. Rev. Lett.*, 97, 187401.

[94] **Widom, M. and Feenstra, R. M.** (2013). Low-energy electron reflectivity from graphene: First-principles computations and approximate models. *Ultramicroscopy*, 130, 101-108.

[95] **Horcas, I., et al.** (2007). WSXM: A software for scanning probe microscopy and a tool for nanotechnology. *Rev. Sci. Instrum.*, 78, 013705.

[96] **Yıldız, D. and Gürlü, O.** (2016). Apparent corrugation variations on moiré patterns on highly oriented pyrolytic graphite. *Materials Today Communications*, 8, 72-78.

[97] **van Wijk, M. M., et al.** (2014). Moiré Patterns as a Probe of Interplanar Interactions for Graphene on h-BN. *Phy. Rev. Lett.*, 113, 135504.

[98] **Hermann, K.** (2012). Periodic overlayers and moir´e patterns: theoretical studies of geometric properties. *J. Phys. Condens. Matter*, 24, 314210.

[99] **Tendeloo, G. V., Landuyt, J. V. and Amelinckx, S.** (1976). The $\alpha \rightarrow \beta$ phase transition in quartz and $AlPO_4$ as studied by electron microscopy and diffraction. *Phys. Status Solidi (a)*, 33, 2, 723-735.

[100] **Moss, G. W.** (1999). Mathematical Models of the Alpha-Beta Phase Transition of Quartz. *Virginia Polytechnic Institute, Blacksburg, Virginia.*

[101] **Heaney, P. J.** (1994). Silica - Physical behavior, geochemistry and materials applications. *Mineralogical Soc. Of America*, Washington, D.C.

[102] **Wood, J. D., et al.** (2011). Effects of Polycrystalline Cu Substrate on Graphene Growth by Chemical Vapor Deposition. *Nano Lett.*, 11, 4547-4554.

[103] **Meyer, E. and Gnecco, E.** (2007). Fundamentals of Friction and Wear. *Nanoscience and Technology, Springer*, Berlin.

[104] **Egberts, P., et al.** (2014). Frictional Behavior of Atomically Thin Sheets: Hexagonal-Shaped Graphene Islands Grown on Copper by Chemical Vapor Deposition. *ACS Nano*, 8, 5, 5010-5021.

APPENDICES

APPENDIX A: User manual for CVD applications.

APPENDIX B: Calculation regarding silicon amount on copper sample (Sample set: S6).

APPENDIX C: AP-CVD grown few layer graphene on Nickel foils.

APPENDIX A

1- Copper foils are cut in desired sizes, and placed in quartz tube.
2- Fans are plugged in. (two of them for cooling input and output flanges, one of them for cooling furnace electronics)
3- Water cooling system is switched on.
4- AP or LP output line is plugged according to the application pressure.
    a. For AP-CVD applications;
        i. Be sure that the bubbler is connected to the system correctly and exhaust line goes to a safe place outside of the laboratory.
    b. For LP-CVD applications;
        i. Be sure that the pump is connected to the system correctly and exhaust line goes to a safe place outside of the laboratory.
        ii. Once the system is fully closed, pump is ready to operate.
        iii. Switched on the pressure gauge control system to read pressure.
        iv. Pump the system until the base pressure reach to 10^{-2} mbar range.
5- MFC control unit is switched on and software is started. (Please ask for username and password.)
6- COM connection is made between MFC controller unit and computer. (from software; Tools > Communication > COM4)
7- Select the Run tab from software and then pick the desired Task.
8- Valves of the main gas tanks is turned on.
9- Output pressure is regulated to 1 bar maximum.
10- H_2 and CH_4 gases are purged for few second.
11- Furnace is turned on by pressing green button.
12- Temperature is set to 400°C by using ↑ and ↓ buttons.
13- Heating is started by pressing * and ↑ buttons simultaneously and then pressing red button.
14- CVD task is started by clicking Run on the software.
15- After 20 mins from starting the heating, temperature is setted to 650°C. (to do that, heating must be stopped first by pressing * and ↓ buttons simultaneously. After the new temperature is setted, heating must be started again).
16- After 35 mins from starting the heating, temperature is setted to 1000°C (or desired process temperature).
17- After the CH_4 flow stopped, heating must be stopped by pressing * and ↓ buttons simultaneously and then pressing red button.
18- When the temperature is decreased to around 200°C, furnace can be splitted to fast cooling down to room temperature.
19- To replace the samples, first gas flow must be stopped by using software.
20- After the gas flow stopped, all valves are turned off.
21- Output line is unplugged to replace the samples.
    a. For AP-CVD applications;
        i. Unplug the output line and replace the samples.
    b. For LP-CVD applications;
        i. Continue to release Argon inside the champer and close the valve on the output line to isolate chamber from pump.
        ii. Once it is isolated, pump is ready to switched off.

iii. After the pump is switched off, unplug the output line and replace the samples. (Do not forget to stop Argon flow.)

22- Fans are switched off.
23- Water cooling system is turned off.
24- MFC controller unit is switched off.
25- Furnace is turned off.

APPENDIX B

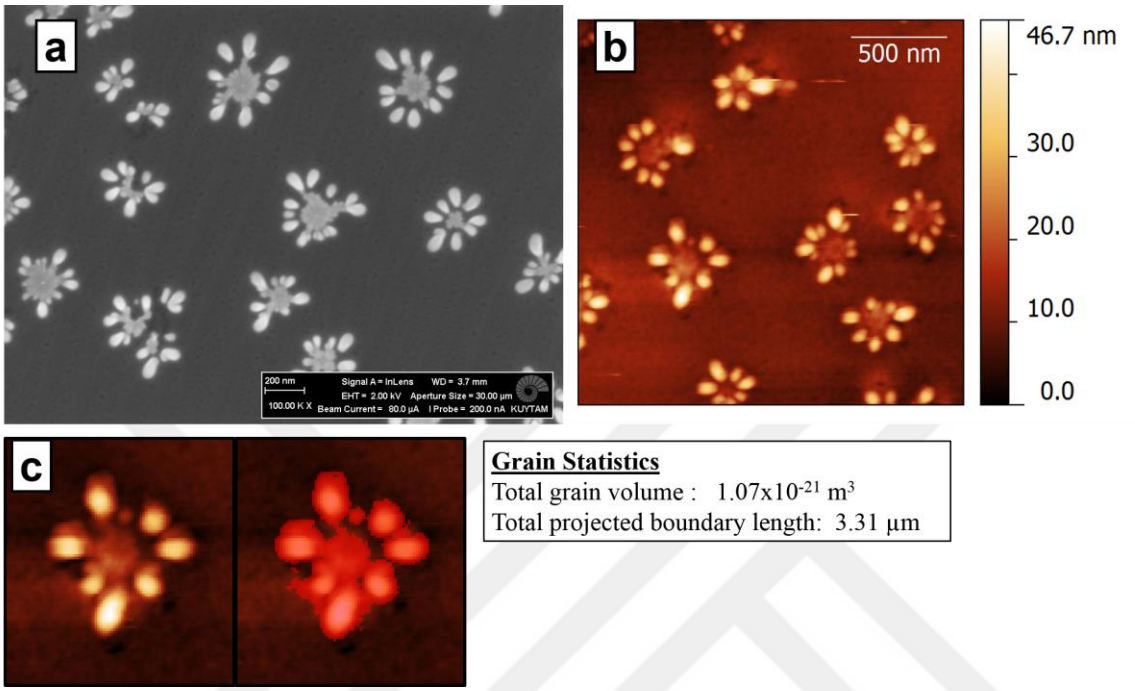

Figure B.1: (a) SEM image of silicon particles on copper foil (Sample set: S6). (b, c) AFM topography maps. Total volume of particles were calculated by Gwyddion software. Total grain volume of masked area in section (c) is written in Grain Statistic section.

Since there are 14 individual particles in SEM image (Figure B 1 a), total volume of the particles in image is;

$$V_{total\ Si} = 15x10^{-15}cm^3$$

And by multiplying the total volume by density of silicon ($2{,}32\ g/cm^3$), we obtain approximate mass of silicon in the SEM image;

$$m_{total\ Si} = 34{,}8x10^{-15}g$$

The total area of SEM image in Figure B 1 (a) is;

$$A_{SEM} = 5{,}56\ \mu m^2$$

Since the thickness of copper foil is $25\mu m$, total volume of copper foil in SEM image is;

$$V_{total\ Cu} = 139\mu m^3 = 139x10^{-12}cm^3$$

And by multiplying the total volume by density of copper ($8{,}96\ g/cm^3$), we obtain approximate mass of copper in the SEM image;

$$m_{total\ Cu} = 1245x10^{-12}g$$

To obtain how much silicon consist on the surface in SEM image in ppm unit;

$$\frac{m_{total\ Si}[mg]}{m_{total\ Cu}[kg]} = 27{,}9\ ppm$$

APPENDIX C

Table C.1: Table of growth conditions.

Sample Group	Heating & Annealing Atmos.(H_2:Ar) [sccm]	Anneal time [min]	Growth Atmos. (H_2:Ar:CH_4) [sccm]	CH_4 Dosing time [min]	Cooling Atmos. (H_2:Ar) [sccm]
N1	500:500	35	100:500:10	5	100:500
N2	500:500	35	100:500:5	5	100:500
N3	500:500	35	1000:500:10	5	1000:500

Initials experiments for AP-CVD graphene growth on Ni foils were shown in Table C 1 with names of sample groups. All sample sets were annealed under same conditions at 950 °C.

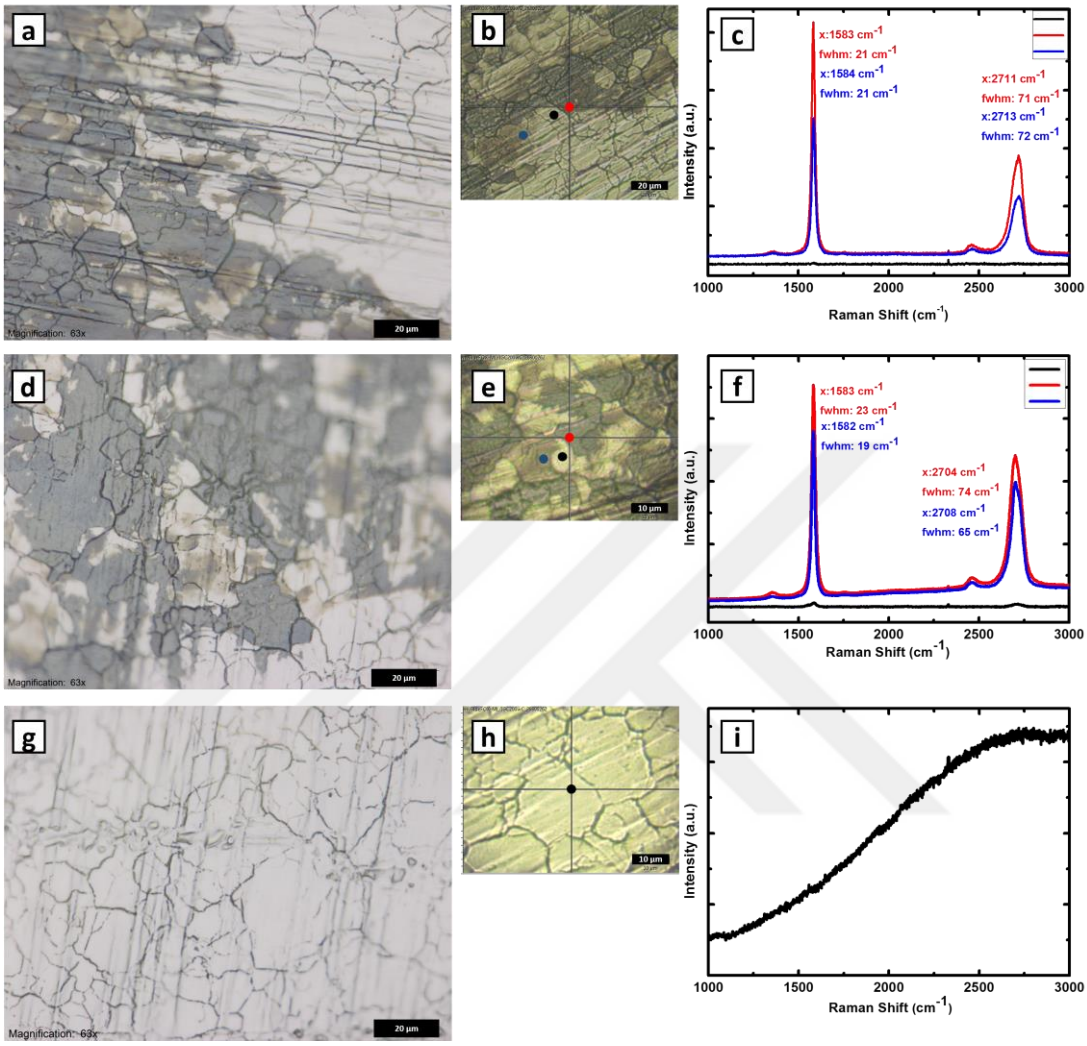

Figure C.1: Optical images of sample sets (a) N1, (d) N2 and (g) N3. Raman spectra of sample sets (c) N1, (f) N2 and (i) N3. (b, e, h) The points that Raman spectroscopy measurements performed are shown on optical images.

For sample sets N1 and N2, we observed that both dark gray and brown areas corresponds to multilayer graphene coverage, while there is no graphene formation on light gray areas. Center and full width at half maximum of G and G' peaks are approximately same for both dark gray and brown areas. The only difference is that Raman signal is more intense on dark gray area than brown area. Since the difference between sample set N1 and N2 is methane dosing, we did not observed any apperent difference depending on methane flowrate under this conditions. In the sample set N3,

we increased the hydrogen flow to 1000 sccm during growth stage. This resulted that graphene formation is prevented.

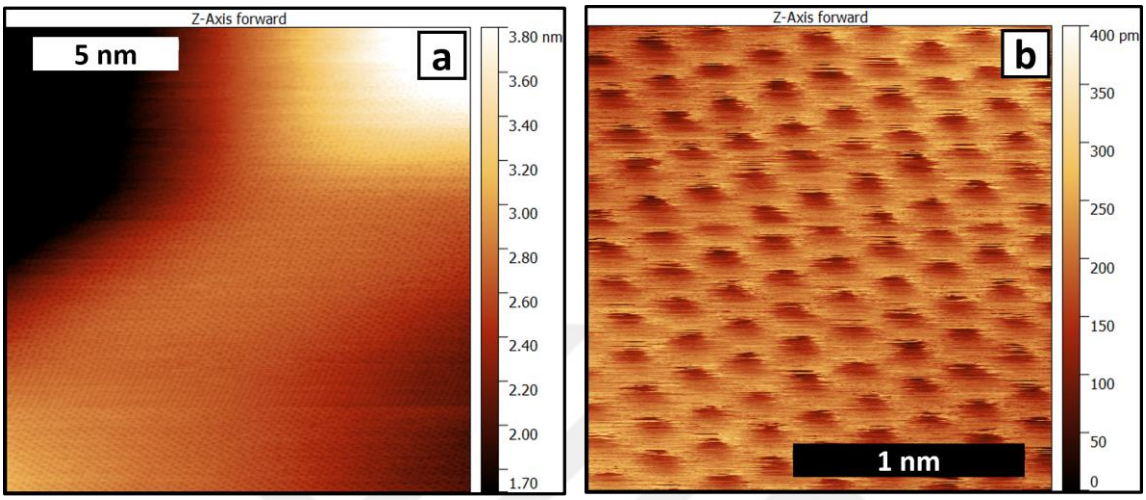

Figure C.2: (a, b) STM topography maps of sample set N1. (Tunneling parameters were V: 500 mV, I: 500 pA)

CURRICULUM VITAE

Name Surname **:** Umut Kamber

Place and Date of Birth **:** İstanbul, 22.10.1991

e-mail **:** kamberu@itu.edu.tr

EDUCATION **:**

- **B.Sc.** **:** 2015, Istanbul Technical University, Faculty of Science and Literature, Physics Engineering

PUBLICATIONS AND PRESENTATIONS ON THE THESIS:

- Kamber U., Kıncal C., Yağcı B., Birer Ö., Gürlü O., (in preparation). Formation of Silicon-Oxide Fractals During Chemical Vapor Deposition Growth of Graphene on Copper Foils.

- Kamber U., Kıncal C., Gürlü O., (in preparation). Lateral Force Microscopy Study on Silicon-Oxide Fractals at Graphene-Copper Interface.

- Kamber U., Kıncal C., Peksu E., Arslan G. B., Yıldız D., and Gürlü O., 2014: Investigation of dendritic structures forming during chemical vapour deposition growth of graphene. NanoTR10 - 10th Nanoscience and Nanotechnology Conference, June, İstanbul, Turkey.

- Kamber U., Kıncal C., Çiftçi H. T., Zengin B., Yıldız D., and Gürlü O., 2015: Interaction between polycrystalline copper substrate and graphene during atmospheric Chemical Vapor Deposition. 79th Annual Meeting of the DPG and DPG Spring Meeting, March, Berlin, Germany.

- Kamber U., Kıncal C., Yağcı B., Birer Ö., and Gürlü O., 2015: Contamination induced defect formation during Chemical Vapor Deposition of graphene and the formation of silicon dendrites. 79th Annual Meeting of the DPG and DPG Spring Meeting, March, Berlin, Germany.

- Kamber U., Kıncal C., Yağcı B., Birer Ö., and Gürlü O., 2015: Dendritic Silicon-oxide clusters forming on CVD grown Graphene. The International Conference on Understanding and Controlling Nano and Mesoscale Friction, June, İstanbul, Turkey.

- Kamber U., Kıncal C., and Gürlü O., 2016: Dendritic and Point-like Silicon-oxide clusters forming under CVD grown graphene on copper. 611. WE-Heraeus-Seminar: Mechanisms of Tribology, March, Bad Honnef, Germany.

- Kamber U., Kıncal C., and Gürlü O., 2016: Fractal structure formation at the graphene-copper interface during Chemical Vapor Deposition: A nanoscale friction perspective. NanoTR12, 12th Nanoscience and Nanotechnology Conference, June, İstanbul, Turkey.

- Kamber U., Kıncal C., Yağcı B., Birer Ö., and Gürlü O., 2016: Formation of Fractal Structures at the Graphene-Copper Interface During Chemical Vapor Deposition. GRM-2016 - Graphene & Related Materials Conference, July, Ankara, Turkey.

- Kamber U., Kıncal C., and Gürlü O., 2016: Friction Force Microscopy Study on Fractal Structures at the Graphene-Copper Interface. GRM-2016 - Graphene & Related Materials Conference, July, Ankara, Turkey.